# The influence of a rock glacier on the riverbed hydrological system

- Bastien Charonnat<sup>1,6,7</sup>, Michel Baraer<sup>1,6,7</sup>, Eole Valence<sup>2,6</sup>, Janie Masse-Dufresne<sup>1,6,7</sup>, Chloé Monty<sup>3</sup>,
- Kaiyuan Wang<sup>4</sup>, Elise Devoie<sup>5</sup>, Jeffrey M. McKenzie<sup>2</sup>
- <sup>1</sup>Hydrology, Climate and Climate Change laboratory École de technologie supérieure (ÉTS), Montreal, Quebec, Canada
- <sup>2</sup> Department of Earth and Planetary Science McGill University, Montreal, Ouebec, Canada
- <sup>3</sup> Department of Earth Sciences Simon Fraser University, Burnaby, British Columbia, Canada
- <sup>4</sup> Department of Earth, Environmental & Planetary Sciences Brown University, Providence, Rhode Island, United States 9
  - <sup>5</sup> Civil Engineering department Queen's University, Kingston, Ontario, Canada
- 10 <sup>6</sup> GEOTOP (Research Centre on the Dynamics of the Earth System), Montreal, Quebec, Canada 11
  - <sup>7</sup>CentrEau (Quebec Research Water Centre), Quebec City, Quebec, Canada
- 13 Correspondence to: Bastien Charonnat (bastien.charonnat.1@ens.etsmtl.ca)

#### Abstract

12

14

17

23

25

26

- 15 Climate change is accelerating cryosphere degradation in mountainous regions, and altering hydrological and
- 16 geomorphological dynamics within deglaciating catchments. Among cryospheric features, rRock glaciers, which degrade
  - slowermore slowly than glaciers, can exert<del>providing</del> a prolongedsustained influence on water resources in alpine watersheds.
- 18 This study investigates both the role of direct and indirect influences of a rock glacier interacting withou the Shár Shaw Tagà
- 19 River (Grizzly Creek) riverbed in the St. Elias Mountains (Yukon, Canada). We applied using a unique multimethod approach
- 20 that integrates combining hydro-physicochemical and isotopic characterization, drone-based thermal infrared (TIR) imagery,
- 21 and visible time-lapse (TL) imagery.
- 22 -Results revealassess that the rock glacier's geomorphic and thermal properties constrain the riverbed and its underlying
  - alluvial aquifer, driving shallow groundwater resurgence, due to their geomorphic properties, can constrict riverbeds and
- 24 alluvial aquifers, and control shallow groundwater flow, leading to notable changes in channel structure and groundwater
  - discharge. These indirect disruptions promote downstream cryo-hydrological processes by facilitating aufeis formation and
  - modifying the physicochemical properties of surface water<del>treamflow</del>. In contrast, direct hydrological influence from the rock
- 27 glacier's internal drainage system to downstream surface waters appears minimal. This configuration is transitional, as the
- 28 constraint imposed by ground ice is expected to diminish with progressive permafrost degradation.
- 29 Overall, this study identifies the critical yet transient role of rock glaciers in alpine hydrology. Beyond their internal
- 30 hydrological behaviour, they shape catchment hydrology through geomorphic controls. Our findings highlight the need to
- 31 account for indirect effects when evaluating hydrological dynamics in deglaciating catchments. Additional findings highlight
- 32 the critical role of rock glaciers and proglacial systems in connecting mountain cryosphere and deep groundwater systems,
- 33 with consequent implications for mountain hydrology and water resources.

#### 1. Introduction

34

35

64

65

36 resources essential for the sustainability that sustain of downstream ecosystems and communities. With rising global 37 temperatures, high mountain areas are experiencing accelerated deglaciation, characterized by glacial retreat and permafrost 38 thaw (Hock et al., 2019). These processes drive rapid geomorphological and hydrological reconfigurations in proglacial 39 systems (Carrivick and Heckmann, 2017). Understanding the impacts of how cryosphere degradation affects on mountain 40 hydrology and hydrogeology is therefore essential for predicting future water availability (Hayashi, 20220; van Tiel et al., 41 2024), in these regions. Recently, the connectivity between the cryosphere and groundwater has been identified as a critical 42 issue in mountain hydrology, directly influencing water resource sustainability under changing climatic conditions (van Tiel 43 et al., 2024). 44 In proglacial systems, riverbeds and outwash plains serve as critical hydrogeological components, sustaining baseflow and 45 aquatic habitats (Käser and Hunkeler, 2016; Müller et al., 2024). However, the recharge and discharge dynamics of alluvial 46 groundwater systems are intrinsically linked to upstream and adjacent cryospheric features (e.g., glaciers, seasonal snowpacks, 47 etc.: Müller et al., 2024), as evidenced by aufeis formation. Aufeis, or icings, are layered ice formations that develop in winter 48 when groundwater outflows persist under sub-zero temperatures for several months (Ensom et al., 2020). These formations can occur due to upwellings of groundwater encountering impermeable permafrost (Terry et al., 2020), with channel 49 50 constriction further promoting their formation (Wainstein et al., 2014; Liu et al., 2021). In mountain environments, aufeis 51 formations are common in outwash plains and are generally supplied by groundwater and meltwater from surrounding 52 cryospheric sources (Chesnokova et al., 2020; Mallinson et al., 2019; Wainstein et al., 2014). 53 Among cryospheric features, rock glaciers degrade the slowest, continuing to influence hydrology long after glaciers have 54 retreated more slowly than glaciers, allowing them to exert a prolonged influence on hydrological processes as glaciers retreat 55 (Bolch and Marchenko, 2009; Harrison et al., 2021; Jones et al., 2021). Despite growing recognition of their hydrological 56 importance, rock glaciers remain understudied compared to glaciers, particularly concerning their roles in deglaciating 57 catchments (Jones et al., 2019). Rock glaciers are tongue-shaped landforms composed of rocky debris and ice, which creep 58 due to the deformation of the ice-debris matrix, concentrated in the shear horizon (Arenson et al., 2002). They are commonly 59 found in high mountain environments and occur in both discontinuous and continuous permafrost zones (Barsch, 1996). While 60 existing studies primarily focus on the internal hydrological behavior of rock glaciers, research addressing their broader 61 catchment-scale implications remains limited (Jones et al., 2019). 62 Historically, research on rock glaciers has focused primarily on two aspects: their hydrological behaviour, particularly their 63 direct influence on catchment hydrology, and their geomorphological dynamics.

Climate change is profoundly transforming mountain regions, where the cryosphere hasplays a critical role in regulating water

Rock glaciers have been shown to In this study, we differentiate between direct hydrological influence (i.e., related to rock

glacier internal hydrological processes and resulting outflows) and indirect hydrological influence (i.e., arising from external

66 processes linked to rock glacier dynamics, such as geomorphic obstruction of a riverbed, limiting hydraulic conductivity and 67 potentially altering surface and shallow groundwater flow patterns). 68 Direct hydrological influence of rock glaciers involves buffering catchment surface waters discharge throughout the year, by 69 sustaining baseflow during dry periods and attenuating discharge response to intense precipitation events due to their internal 70 structurepeaks (Bearzot et al., 2023; Reato et al., 2022; Wagner et al., 2021). Their-A rock glacier's hydrological behaviour is 71 closely tied to its internalthe distribution of frozen and liquid water within them (Harrington et al., 2018; Wagner et al., 2016; 72 Winkler et al., 2016). Unfrozen layers in summer can act as reservoirs and conduits for water flow (Halla et al., 2021; 73 Harrington et al., 2018; Navarro et al., 2023; Wagner et al., 2020). In addition to liquid water, intact rock glaciers (i.e., 74 containing frozen content) store significant volumes of solid water as interstitial or massive ice (Chakravarthi et al., 2022; 75 Halla et al., 2021; Jones et al., 2018; Wagner et al., 2021). However, internal ice melt typically contributes only minimally to 76 total rock glacier discharge (Arenson et al., 2022). RIn addition to modulating discharge, rock glaciers also directly influence 77 downstream water quality by increasing solute concentrations (Colombo et al., 2018; Colombo et al., 2019; Schreder et al., 78 2023; Engel et al., 2019; Wanner et al., 2023; Zarroca et al., 2021) and cooling stream temperatures (Bearzot et al., 2023; 79 Brighenti et al., 2019; Colombo et al., 2020). The physicochemical impact of rock glacier outflows is particularly pronounced 80 at the catchment scale when compared to catchments lacking glacial or periglacial landforms (Brighenti et al., 2023; Clow et 81 al., 2021; Del Siro et al., 2023; Gammons et al., 2021; Robinson et al., 2022). 82 While much of the literature focuses on the downstream effects of rock glacier outflows (e.g., Brighenti et al., 2023; Robinson 83 et al., 2022; Wagner et al., 2016; Wagner et al., 2021), their influence on the hydrogeomorphology of riverbeds and outwash 84 plains remains understudied. RIn addition, rock glaciers can exert indirect hydrological effects, as they are dynamic landforms 85 that ean advancemay advance, constrain, or even and dam riverbeds, potentially forming ponds, as Such effects have been 86 reported in High Asia (Blöthe et al., 2019; Falatkova et al., 2020; Hewitt, 2014) and the Alps (Colombo et al., 2020). 87 Furthermore, topographic changes driven by glacial retreat and paraglacial processes can force channel confinement (Marren 88 and Toomath, 2014). Climate change has intensified rock glacier movement (Delaloye et al., 2010; Kummert et al., 2019; 89 PERMOS, 2019), sometimes causing destabilization (Marcer et al., 2021) and channel disruption (Sorg et al., 2015). 90 Additionally, sudden mass movements, such as the catastrophic collapse of rock glacier lobes, have triggered debris flows with 91 downstream geomorphic impacts (Bodin et al., 2015; Scotti et al., 2017). Riverbeds and outwash plains play an important role 92 in sustaining baseflow and aquatic habitats (Käser and Hunkeler, 2016; Müller et al., 2024). However, to our knowledge, the 93 indirect hydrological effects of rock glacier dynamics have not yet been assessed or compared with the direct effects of rock 94 glaciers. The hydrological and geomorphic disturbances caused by advancing rock glaciers in valley systems are particularly 95 notable, given the critical role of riverbeds and outwash plains in sustaining water resources. Despite recent studies (e.g., 96 Falatkova et al., 2020; Wagner et al., 2021), research on the interactions between rock glaciers, the adjacent cryosphere, surface 97 waters, and groundwater flow within valley systems is still underexplored.

This study examines the influence of rock glaciers on surface and shallow groundwater flow within alpine riverbed hydrological systems. Specifically, it focuses on characterizing water fluxes in a section of the Shár Shaw Tagà catchment (St. Elias Mountains, Yukon, Canada) that is constrained by a rock glacier. We hypothesize that the rock glacier modulates interactions between surface water and shallow groundwater, thereby affecting the overall functioning of the riverbed system. To investigate these interactions, we employed a multimethod approach that was progressively refined as our observations and understanding of the system evolved: The objective of this study is to address this research gap by simultaneously examining the direct and indirect hydrological influences of a rock glacier extending into a valley floor. Specifically, we aim to elucidate the underlying processes and anticipate the potential evolution of the system. We focus on surface water and shallow groundwater fluxes within a section of the Shár Shaw Tagà River in the St. Elias Mountains, Yukon, Canada, where the riverbed is constrained by the rock glacier. To reach this objective, we use a multimethod approach that combines observational techniques and naturel tracer analyses in two steps:

- Monitoring and surveying of groundwater exfiltration, hypothesized to occur within the constrained river section, and
  causing significant outflows and winter aufeis formation. To assess the presence of important groundwater outflows
  in this section, we use drone-based thermal infrared (TIR) surveys, time-lapse monitoring and radon activities
  measurements.
- Physico-hydrochemical characterization to distinguish outflows associated with either the direct or the indirect influences of the rock glacier. We use synoptic sampling and hydrochemical analyses to characterize distinct water sources and their relative contributions.

- 1. We hypothesized that the rock glacier influences the formation of aufeis on the downstream outwash plain. To test this, we used time-lapse camera monitoring to track the development of aufeis and to identify the location and timing of winter outflows.
- 2. Given the rock glacier's position at the outlet of a subcatchment and the lack of significant surface outflow, we hypothesized that it drains the subcatchment and contributes to river discharge via groundwater exfiltration. To assess this, we conducted a spring inventory, followed by a physico-hydrochemical characterization of springs and streams across the subcatchment. This allowed us to trace water sources and evaluate the rock glacier's influence on stream composition.
- 3. Building on the previous findings, we hypothesized that a specific section of the riverbed serves as a major zone of groundwater exfiltration. To identify and map these zones, we conducted drone-based thermal infrared (TIR) surveys, enabling us to delineate areas of groundwater emergence and assess their spatial extent and relative magnitude.

The novelty of this research lies in its focus on the its simultaneous assessment of direct and indirect hydrological influences impacts of a rock glacier on catchment hydrologya rock glacier—particularly in the absence of a visible, well-defined outflow. By integrating hydrological, hydrogeological, and geochemical methods, this study Our findings highlightadvances our

**Formatted:** List Paragraph, Numbered + Level: 1 + Numbering Style: 1, 2, 3, ... + Start at: 1 + Alignment: Lef Aligned at: 0,63 cm + Indent at: 1,27 cm

132 provide provides insights with broader applicability applicable to similar environments worldwide. 133 2. Study site 134 Shár Shaw Tagà, meaning Grizzly Creek in the Southern Tutchone indigenous language, is a 32 km² glacierized catchment 135 located within the traditional lands of the Kluane First Nation and the White River First Nation (Fig. 1a). It also lies within 136 the boundaries of Kluane National Park and Reserve in the St. Elias Mountains, southwestern Yukon Territory, Canada 137 (61°05'13" N, 139°07'18" W). The eastern flank of the St. Elias Mountains experiences a dry subarctic climate, characterized 138 by annual precipitation ranging from 300 mm yr<sup>-1</sup> to 500 mm yr<sup>-1</sup> and a mean annual temperature between -8 °C and -12 °C 139 (Wahl et al., 1987). 140 Publications prior to 2024 referred to the area by the toponym "Grizzly Creek" rather than Shár Shaw Tagà. The upper Shár 141 Shaw Tagà catchment (Fig. 1b) contains eight glaciers, the largest of which is G-A1, covering an area of 3.2 km<sup>2</sup>. Faults are 142 inferred along the valley floor (Dodds and Campbell, 1992). Due to its heavily fractured bedrock lithology and steep slopes, 143 the valley is characterized by significant mass wasting processes and depositional features, including nine previously identified 144 rock glaciers (Johnson, 1978; Evin et al., 1997). Between 1974 and 1997, Johnson participated to a series of geomorphological 145 studies on the valley (Johnson, 1974; 1978; 1980; 1983; 1986; 1992; Evin et al., 1997), providing detailed descriptions of its 146 landforms. The geomorphological identification and landform naming for these features, as established in Johnson's works, 147 are adopted in this study to characterize the geomorphological setting. 148 The significance of ground ice landforms in the valley has prompted recent investigations, including a study on buried ice 149 detection using ground-penetrating radar (GPR) in rocky and steep terrains (Tjoelker et al., 2024). Publications prior to 2024 150 referred to the area by the toponym "Grizzly Creek" rather than Shar Shaw Taga. Of these nine rock glaciers identified by 151 Johnson and Evin et al. (1978; 1997), seven extend into the riverbed along the valley floor, with some exerting considerable

understanding of the complex and dynamic role of rock glaciers play in alpine catchmentwatershed dynamics systems, and

131

152

153

geomorphological constraints on the stream.

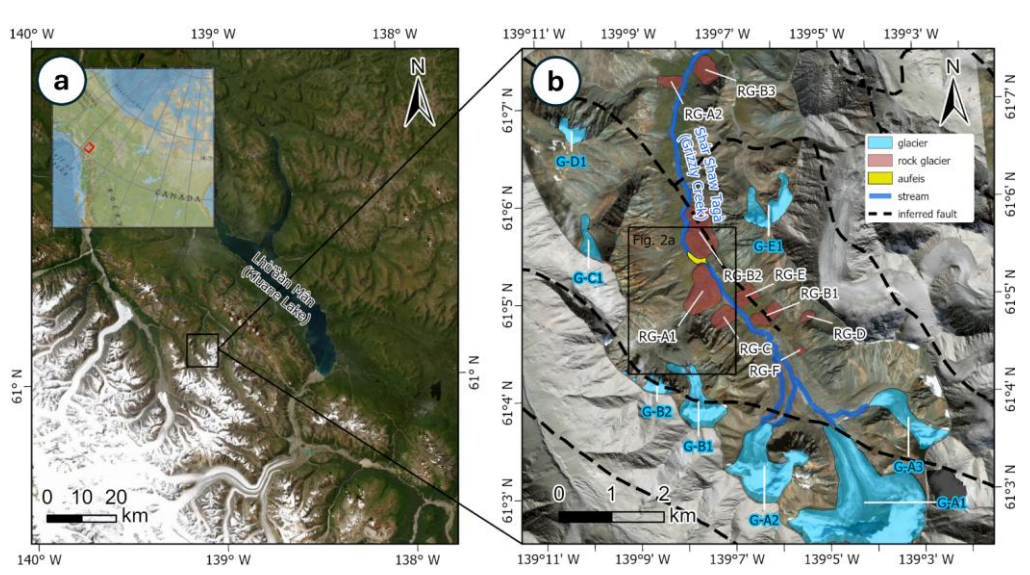


Fig. 1: (a) Overview map showing the location of the Shár Shaw Tagà valley in southwestern Yukon, Canada. (b) Enlarged view of the study area from panel (a), highlighting key geomorphological features. The black frame outlines the extent of the map shown in Fig. 2a. ArcticDEM data: Polar Geospatial Center (Porter et al., 2023). Basemap credits: Esri.

The present study investigates the hydrological influence of focuses on the RG-A1 rock glacier, located on the western side of the upper Shár Shaw Tagà valley. The front of RG-A1 advances in the valley, constraining the Shár Shaw Tagà River against the opposing talus slope. RG-A1, first identified by Johnson (1978), spans elevations between 1700 and 1850 m a.s.l. The southern lobes of RG-A1 appear older, characterized by vegetation cover and a smoother frontal morphology, while the northern lobes are younger, with sparse or absent vegetation, sharper forms, and a steeper front (Johnson, 1978). A frozen layer, Based on geophysical surveys, Evin et al. (1997) report a 20 to 40 m thick frozen layer as well as the presence of massive ice lenses at depth was detected in RG-A1 during a previous geophysical study, which also suggested the presence of massive ice lenses at depth (Evin et al., 1997). The front of RG-A1 advances in the valley, constraining the Shár Shaw Tagà River against the opposing talus slope. Although previous studies did not classify the opposing talus slope as a rock glacier, it is suspected to be a protalus rampart (or small active rock glacier) based on environmental and topographic criteria outlined in Scapozza (2015), such as the absence of an upstream permanent snow field, the presence of coarse boulders in the upslope area, a steep front with exposed fine sediments, and its juxtaposition and superimposition to other rock glaciers.

173 The outwash plains upstream and downstream of RG-A1 are separated by a "narrow section" of the Shár Shaw Tagà River, 174 which can be divided into two subsections: N1 and N2 (Fig. 2). N1 extends from the outlet of the upstream outwash plain to a 175 bedrock outcrop visible on the opposite talus slope to RG-A1. N2 extends from this bedrock outcrop to the outlet of the "narrow 176 section", where the rivers reachesenters the downstream outwash plain. Although previous studies did not classify the talus 177 slope opposed to RG-A1 as a rock glacier, it is suspected to be a protalus rampart (or small active rock glacier) based on 178 environmental and topographic criteria outlined in Scapozza (2015). We noted the absence of an upstream permanent snow 179 field, the presence of coarse boulders in the upslope area, a steep front with exposed fine sediments, and a juxtaposition and 180 superimposition to other rock glaciers. 181 An aufeis forms in winter in the downstream outwash plain, as confirmed through field studies since 2018 and satellite imagery. 182 No aufeis has been detected in the upstream outwash plain during this period. 183 In 1974, Johnson (1978) observed that meltwater drained into a sinkhole located in the rooting zone of RG-A1 (at 184 approximately 1850 m a.s.l.), with no major resurgence observed at itsthe front (at 1700 m a.s.l.). In 1975, a new sinkhole was 185 observed upstream of the first one, and a significant resurgence was reported on the northern part of RG-A1. Dry channels on 186 the surface of RG-A1 in 1975 were interpreted by Johnson as abandoned surface drainage pathways, highlighting the dynamic 187 and variable hydrological behaviour of RG-A1. Field observations by our team from 2018 to 2023 indicate no significant 188 visible outlet from the rock glacier, despite its position downstream of an 8 km² subcatchment containing the G-B1 and G-B2 189 glaciers. The only visible outlets consist of low-discharge springs around the RG-A1 front, particularly concentrated along the 190 N1 subsection. The lack of surface outflow from the rock glacier suggests subsurface connectivity with the Shár Shaw Tagà River. 192 During low-discharge periods, such as in June 2023, we observed infiltration of Shár Shaw Tagà River water into the riverbed, 193 leaving the channel dry before the outwash plain upstream of RG-A1. Flow re-emerged in the N1 subsection, close to the rock 194 glacier's front, visually sustained by springs and seepage. Additional subsurface flow paths are evident in winter through aufeis 195 formation in the downstream outwash plain, documented by field observations since 2018 and on satellite imagery, while no 196 aufeis has been detected upstream between 2018 and 2023. Aufeis (or icings) are layered ice accumulations that develop when 197 groundwater outflows persist under sub-zero temperatures (Ensom et al., 2020). 198 The configuration of RG-A1, which constrains the riverbed, together with these groundwater observations in the "narrow 199 section," supports our hypothesis that the rock glacier exerts both direct and indirect hydrological influence on the riverbed 200 system. Accordingly, our methodology focuses on characterizing the sources and impacts of groundwater exfiltration in this 201 section. Field observations by our research team from 2018 to 2023 confirm the absence of a significant visible outlet from the 202 rock glacier, despite its location downstream of a 8 km<sup>2</sup> subcatchment, consisting of the G-B1 and G-B2 glaciers. The only 203 visible outlets consist of low-discharge springs around the RG-A1 front, particularly concentrated along the N1 subsection. 204 During low-discharge periods such as June 2023, we observed that the water from the Shár Shaw Tagà River infiltrates the riverbed, leaving it dry before entering the outwash plain upstream of RG-A1. However, water was observed to flow again 205

191

within the riverbed in the N1 subsection, visually sustained by springs and seepage. During high-flow periods, the springs emerge directly under the front of RG-A1. In dry periods, like June 2023, the springs shift away from the front and align with the current river level, 10 to 20 m downstream.

210 3. Methods

206

207

208

209

211

212

213

214

215

216

217

218

219

220

221

222

223

224

225

226

227

228

229

230

231

232

233

234

235

236

3.3 TIR survey3.1 Monitoring and surveying of groundwater exfiltration 3.1.2 TIR survey Aerial and handheld thermal infrared (TIR) devices have been demonstrated as effective tools for mapping groundwater discharge into streams (Toran, 2019). Specifically, drone-based TIR technology allows for high spatial resolution observations of surface water-groundwater interactions (Vélez-Nicolás et al., 2021). Two common approaches for TIR surveys were considered: 1) generating stream temperature maps using high-definition TIR image orthomosaics from overlapping images (e.g., Abolt et al., 2018; Casas-Mulet et al., 2020; Rautio et al., 2015), and 2) using TIR videos or real-time scans (handheld or drone-based) to visualize mixing plumes and record GPS coordinates of observed points (e.g., Barclay et al., 2022; Briggs et al., 2016; Iwasaki et al., 2023). Georeferenced thermal maps provide mesoscale coverage but require stable flying conditions, ground control points, and extensive post-processing (Webb et al., 2008). In contrast, TIR video or live scans enable real-time visualization of mixing dynamics at smaller scales (Antonelli et al., 2017). To identify and characterize cold groundwater emergence zones, we adopted the TIR video approach, which relies on relative temperature contrasts between stream water and suspected groundwater inflows rather than precise absolute temperatures. Previous studies have demonstrated that TIR video effectively highlights such contrasts even without embedded temperature scales (Antonelli et al., 2017; Briggs et al., 2016; Iwasaki et al., 2023, 2024). While georeferenced thermal maps provide mesoscale coverage, they require stable flying conditions, ground control points, and extensive post-processing (Webb et al., 2008). In contrast, TIR video or live scans allow for real-time visualization of mixing dynamics in smaller scale areas (Antonelli et al., 2017). Given our goal to identify and characterize groundwater exfiltration zones, we chose the TIR video approach. This method does not require precise absolute temperature but relies instead on relative contrasts between stream water and suspected groundwater inflows. Prior studies (Antonelli et al., 2017; Briggs et al., 2016; Iwasaki et al., 2023; Iwasaki et al., 2024) have shown that TIR video, even without embedded temperature scales, effectively highlights such contrasts. Drone-based TIR video surveys were conducted on 28 June 2024, between 08:00 and 10:00, to maximize the coverage of shaded sections of the stream. The surveys were conducted using a DJI Mavic 3T Enterprise, equipped with a DJI RTK module and a DJI D-RTK 2 mobile station for GNSS base-station support. The Mavic 3T features a 48-megapixel RGB camera with a 24 mm focal length and a 640 × 512-pixel thermal camera with a 40 mm focal length. The drone was manually controlled to

optimize the capture of surface temperatures across wide sections of the Shár Shaw Tagà River, recording both TIR and RGB videos simultaneously. Flight altitudes ranged from 5 to 20 m above ground level with depending on the section. All flights were manually piloted at low altitudes and near-nadir angles to reduce geometric distortion and minimize emissivity-related error (Torgersen et al., 2001; Dugdale et al., 2016). The survey began approximately 180 m upstream of the N1 subsection and ended around 800 m downstream of the N2 subsection (Fig. 2). Due to difficulties in flying over the narrow section, it was surveyed twice at different elevations. The TIR video was visually analyzed to identify cold groundwater exfiltration-water emergence zonesareas using two criteria: 1) a clear contrast between the dominant stream surface temperature and the suspected exfiltration area, with an area larger than 10 cm<sup>2</sup>, and 2) the presence of a turbulent mixing zone at least 1 m in length immediately downstream of the suspected area (flight data and information are available as Supplemental Material in Charonnat and Baraer, 2025). Absolute temperatures were not derived due to the absence of a calibrated color scale in the TIR video; instead, detection relied on qualitative identification of relative temperature differences appearing as visual color contrasts in the TIR video—typically, colder areas appeared as blue-toned patches compared to the green-toned stream and red-toned sunlit boulders. When both criteria were met, the RGB video was used for confirmation. The Shár Shaw Tagà River, originating from glacial melt, has a substantial suspended sediment load, whereas groundwater is nearly free of suspended sediments. This contrast is visible in the RGB video frames. The observed thermal contrasts were consistent with previously measured field temperature differences between springs and stream water, typically >2°C and <6°C (Table S1), and exceeded the uncertainty range of uncorrected thermal imagery under field conditions (Zappa and Jessup, 1998). Finally, images of confirmed cold-water emergence zonesgroundwater exfiltration areas were extracted from the videos for size evaluation. Exfiltration areas from the left bank were labeled TIR-L#, and those from the right bank were labeled TIR-R#.

#### 3.1.21 TL monitoring

237

238

239

240

241

242

243

244

245

246

247

248

249

250

251

252

253

254

255

256

257

258

259

260261

262

263

264

265

266

267

Three Two RGB timelapse (TL) cameras, designated TL1, and TL2 and TL3, were positioned installed above along the right bank of the Shár Shaw Tagà River (TL1 and TL2: 61°5'26" N, 139°7'34" W; TL3: 61°5'12" N, 139°7'13" W; Fig. 2); Fig. 2). TL1, was installed in 2018, monitored focused on the central area of the outwash plain immediately downstream of RG-A1. In 2019, TL2 was added adjacent to TL1, extending its field of view coverage from the upper margin of TL1's eoverage field of view to the outlet of the N2 subsection of the Shár Shaw Tagà River. Finally, TLC3 was added in 2021 on the bedrock outcrop, oriented toward the N1 subsection, with the upstream outwash plain in the background. AllBoth cameras were configured to capture four images daily at 8:00, 11:00, 13:00, and 16:00. VThe visual analysis of the images captured by of the TL eameras imagery involved identifying the signsorigins of surface overflow within the riverbed and on the developing aufeis, as well as and documenting their occurrence of such events throughout the winter, following the protocol outlined by of

Formatted: Normal

268 Chesnokova et al. (2020). Monitoring these overflow events enabled the identification and spatial localization of groundwater
269 outflow points.

#### 3.1.3 Radon activities measurements

Radon (222Rn) serves as a natural tracer to detect groundwater exfiltration in streams (Cartwright and Hofmann, 2016). In June

- 2023, in situ radon activities were measured at two springs exhibiting the most visible discharge within the N1 subsection: S-
- 273 RG8, at the RG-A1's front, and S-RG9A, on the opposite talus slope (Fig. 2). Radon activities were also measured in the Shár
  - Shaw Tagà River at the upstream and downstream ends of the N1 subsection (points S-RUP and S-R1, respectively). A portable
  - RAD7 Radon Monitor (Durridge) was used, coupled with the Rad Aqua accessory (Durridge) for radon degassing. Results are
  - reported in Bq m<sup>-3</sup>

#### 3.22 Physico-hydrochemical characterisation

#### 3.22.1 Sampling and field measurements

Physico-hydrochemical characterisation was undertaken over three—distinct campaigns to capture different hydrological conditions: June 2022, August 2022, and June 2023. These campaigns targeted both the Shár Shaw Tagà River and springs inventoried from 2018 to 2021, capturing different hydrological conditions. The June 2022 campaign coincided with the melt of a late and substantial snowpack. The August 2022 campaign took place during late summer, when glacial ablation was at its peak. The June 2023 campaign was conducted following a winter with reduced snowpack and early snowmelt, after the primary snowmelt phase but before summer glacial ablation commenced, while glaciers remained snow-covered. The three campaigns targeted both the Shár Shaw Tagà River and low-discharge springs along the front of RG-A1 to investigate subsurface connections between the rock glacier and the riverbed (Fig. 2). Additional sites were selected in the proglacial field and in the ice—debris complex of the G-B1 subcatchment, hypothesized to be drained by RG-A1 and therefore potentially contributing to the springs. In these areas, all flowing waters were systematically inventoried and sampled. Samples were categorized into four types (Table A1): glacial outlets from the G-B1 snout (S-GL#), streams in the ice-debris complex located between the G-B1 snout and RG-A1 (S-IDC#), springs at the RG-A1 front and opposite talus (S-RG#), and Shár Shaw Tagà River (S-R#). When possible, sites were sampled multiple times within each campaign to account for diurnal fluctuations in physicochemical parameters.

The physico-chemical characterization focuses on natural tracers' analysis for deciphering the origins of the groundwater outflows. Major and minor ions (Ca<sup>2+</sup>, Mg<sup>2+</sup>, Na<sup>+</sup>, Cl<sup>-</sup>, SO<sub>4</sub><sup>2-</sup>, K<sup>+</sup> and F') were selected for the analysis as their concentrations in water are related to the groundwater residence time and pathways. The natural tracers' analysis includes water stable isotopes too. Field measurements comprehended in situ pH, electrical conductivity (EC, corrected to 25 °C, expressed in µS cm<sup>-1</sup>), and water temperature (°C), adding information about groundwater residence time and the presence of frozen content adjacent to

Formatted: Heading 3

299 98195 multiparameter meter. 300 Field measurements included in situ pH, electrical conductivity (EC, corrected to 25 °C, expressed in uS cm<sup>-1</sup>), and water 301 temperature (°C). Water samples were collected for laboratory analyses. Additionally, in June 2023, in situ radon 302 measurements were performed to further investigate groundwater contributions. Measurements were taken at each sampling 303 site using a calibrated Hanna HI 98195 multiparameter meter. 304 Water sampling followed a synoptic approach for cycles of 1-2 days, avoiding precipitation periods (e.g. Baraer et al., 2009). 305 When possible, sites were sampled multiple times within each campaign to account for diurnal fluctuations in physicochemical 306 parameters. Samples were categorized into four types (Table A1): glacial outlets from the RG-B1 snout (S-GL#), streams in the ice debris complex located between the RG-B1 snout and RG-A1 (S-IDC#), springs at the RG-A1 front and opposite talus 307 308 (S-RG#), and Shar Shaw Taga River (S-R#). Water sampling followed a synoptic approach for cycles of 1-2 days, avoiding 309 precipitation periods (e.g. Baraer et al., 2009). Water samples were filtered using 0.45 µm syringe filters and collected in 50 310 mL HDPE bottles, rinsed three times prior to sampling. Not all sites were sampled ataccessible during each campaign (Table 311 A1), due to various factors (e.g., such as no flow or safety concerns related to snow cover and rockfalls). 312 Results were analyzed following the methodology of Baraer et al. (2015). Samples for major ion analysis were stored in a dark 313 environment at 4 °C until analysis. Major ions (Ca2+, Mg2+, Na+, Cl-, SO4+) and minor ions (K+, F-) were analyzed at the LG2 314 laboratory, École de technologie supérieure (ÉTS), Montreal, Canada. Cation concentrations were measured<del>determined</del> using 315 an inductively coupled plasma optical emission spectrometer (5110 ICP-OES, Agilent), and anion concentrations were 316 measured with an ion chromatograph (Dionex ED50, Thermo Fisher Scientific). Bicarbonate (HCO<sub>3</sub><sup>-</sup>) concentrations were 317 calculated from the charge balance equation, and total dissolved solids (TDS) were derived from the sum of ion concentrations. 318 Stable isotopic composition of the water molecule ( $\delta^{18}$ O and  $\delta^{2}$ H) was measured using a cavity ringdown spectrometer (Picarro 319 L2130-i) at the LG2 laboratory (ÉTS), Montreal, Canada, expressed in % relative to Vienna Standard Mean Ocean Water 320 (VSMOW). Internal reference waters were used for normalization after every three analysis injections. The analytical 321 uncertainty is  $\pm 0.13$  % for  $\delta^{18}O$  and  $\pm 1.5$  % for  $\delta^{2}H$ . The nearest local meteoric water line (LMWL) is established for the 322 Whitehorse area 220 km east of Shár Shaw Tagà (Birks et al., 2004). The LMWL is similar to isotopic compositions found in 323 the Lhù'ààn Mân' (Kluane Lake), 25 km east of Shár Shaw Tagà (Brahney et al., 2010). The LMWL is displayed alongside the 324 analyses results as reference (Fig. 6d, Fig. 7d and Fig. 8d) but we prefer not to assume direct applicability to our data... 325 Radon (222Rn) serves as a natural tracer to detect groundwater exfiltration in streams (Cartwright and Hofmann, 2016). In situ 326 radon activities were measured at four locations in the N1 subsection, including S-RG8 and S-RG9A springs, and at the 327 upstream and downstream ends of the N1 subsection (S-RUP and S-R1, respectively). A portable RAD7 Radon Monitor 328 (Durridge) was used, coupled with the Rad Aqua accessory (Durridge) for radon degassing. Results are reported in Bq m<sup>-3</sup>, 329 with an analytical uncertainty of ± 220 Bq m<sup>-3</sup>. Results were interpreted following the methodology of Baraer et al. (2015). The

groundwater pathways. Measurements for pH, EC and water temperature were taken at each site using a calibrated Hanna HI

298

absolute values of water temperature and EC measured in situ were considered for tracers while means and ranges were used to assess the diversity in physico-chemical composition among the samples for Principal Component analysis (PCA).

# 3.22.2 Principal Component Analysis and clustering

Principal Component Analysis (PCA) was <u>usedemployed</u> to classify the origins of the sampled water and to identify sample groups that influence the chemistry of the Shár Shaw Tagà River. For each of the three sampling campaigns, PCA was performed using a set of independent variables: water temperature, δ<sup>18</sup>O, Na<sup>+</sup>, Mg<sup>2+</sup>, Ca<sup>2+</sup>, and SO<sub>4</sub><sup>2-</sup>. These major ions were selected as they exhibited concentrations above the detection limit in more than 95 % of the samples. Principal components explaining at least 90 % of the total variance were retained for further analysis to ensure the robustness of the PCA.

After conducting PCA, clustering analysis was performed using the k-means algorithm for each campaign (Lloyd, 1982; MacQueen, 1967). This analysis was based on the sample scores derived from the selected principal components. The

MacQueen, 1967). This analysis was based on the sample scores derived from the selected principal components. The maximum number of clusters was set at 25 % of the total number of samples for each campaign, which corresponded to 5, 9 and 7 for the campaigns of June 2022, August 2022, and June 2023, respectively. The algorithm determined the resulting clusters were by associating samples with dominant combinations of variables, thereby highlighting inherent patterns within the dataset.

#### 3.3 TIR survey

Aerial and handheld thermal infrared (TIR) devices have been demonstrated as effective tools for mapping groundwater discharge into streams (Toran, 2019). Specifically, drone-based TIR technology allows for high spatial resolution observations of surface water-groundwater interactions (Vélez-Nicolás et al., 2021). Two common approaches for TIR surveys were considered: 1) generating stream temperature maps using high-definition TIR image orthomosaics from overlapping images (e.g., Abolt et al., 2018; Casas-Mulet et al., 2020; Rautio et al., 2015), and 2) using TIR videos or real-time scans (handheld or drone-based) to visualize mixing plumes and record GPS coordinates of observed points (e.g., Barclay et al., 2022; Briggs et al., 2016; Iwasaki et al., 2023).

While georeferenced thermal maps provide mesoscale coverage, they require stable flying conditions, ground control points, and extensive post-processing (Webb et al., 2008). In contrast, TIR video or live scans allow for real-time visualization of mixing dynamics in smaller-scale areas (Antonelli et al., 2017). Given our goal to identify and characterize groundwater exfiltration zones, we chose the TIR video approach. This method does not require precise absolute temperature but relies instead on relative contrasts between stream water and suspected groundwater inflows. Prior studies (Antonelli et al., 2017; Briggs et al., 2016; Iwasaki et al., 2023; Iwasaki et al., 2024) have shown that TIR video, even without embedded temperature scales, effectively highlights such contrasts.

Drone-based TIR video surveys were conducted on 28 June 2024, between 08:00 and 10:00, to maximize the coverage of shaded sections of the stream. The surveys were conducted using a DJI Mayic 3T Enterprise, equipped with a DJI RTK module and a DJI D-RTK 2 mobile station for GNSS base-station support. The Mayie 3T features a 48-megapixel RGB-camera with a 24 mm focal length and a 640 × 512-pixel thermal camera with a 40 mm focal length. The drone was manually controlled to optimize the capture of surface temperatures across wide sections of the Shar Shaw Taga River, recording both TIR and RGB videos simultaneously. Flight altitudes ranged from 5 to 20 m above ground level, depending on the section. All flights were manually piloted at low altitudes and near-nadir angles to reduce geometric distortion and minimize emissivity-related error (Torgersen et al., 2001; Dugdale et al., 2016). The survey began approximately 180 m upstream of the N1 subsection and ended around 800 m downstream of the N2 subsection (Fig. 2). Due to difficulties in flying over the narrow section, it was surveyed twice at different elevations. The TIR video was visually analyzed to identify cold groundwater exfiltration areas using two criteria: 1) a clear contrast between the dominant stream surface temperature and the suspected exfiltration area, with an area larger than 10 cm<sup>2</sup>, and 2) the presence of a turbulent mixing zone at least 1 m in length immediately downstream of the suspected area (flight data and information are available as Supplemental Material in Charonnat and Baraer, 2025). Absolute temperatures were not derived due to the absence of a calibrated color scale in the TIR video; instead, detection relied on qualitative identification of relative temperature differences appearing as visual color contrasts in the TIR video—typically, colder areas appeared as blue-toned patches compared to the green-toned stream and red-toned sunlit boulders. When both criteria were met, the RGB video was used for confirmation. The Shar Shaw Tagà River, originating from glacial melt, has a substantial suspended sediment load, whereas groundwater is nearly free of suspended sediments. This contrast is visible in the RGB video frames. The observed thermal contrasts were consistent with previously measured field temperature differences between springs and stream water, typically >2°C and <6°C (Table S1), and exceeded the uncertainty range of uncorrected thermal imagery under field conditions (Zappa and Jessup, 1998). Finally, images of confirmed groundwater exfiltration areas were extracted from the videos for size evaluation. Exfiltration areas from the left bank were labeled TIR-L#, and those from the right bank were labeled TIR-R#.

360

361

362

363

364

365

366

367

368

369

370

371

372

373

374 375

376

377

378

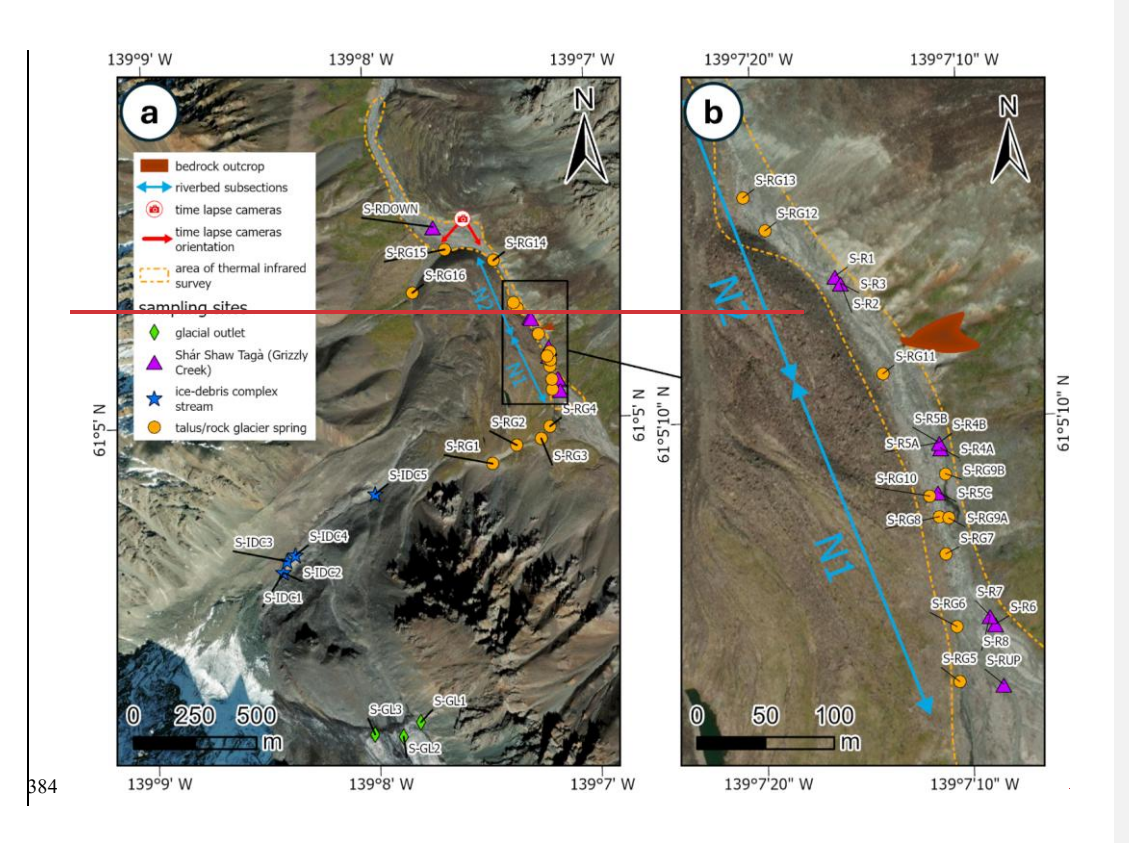
379

380

381

382

383



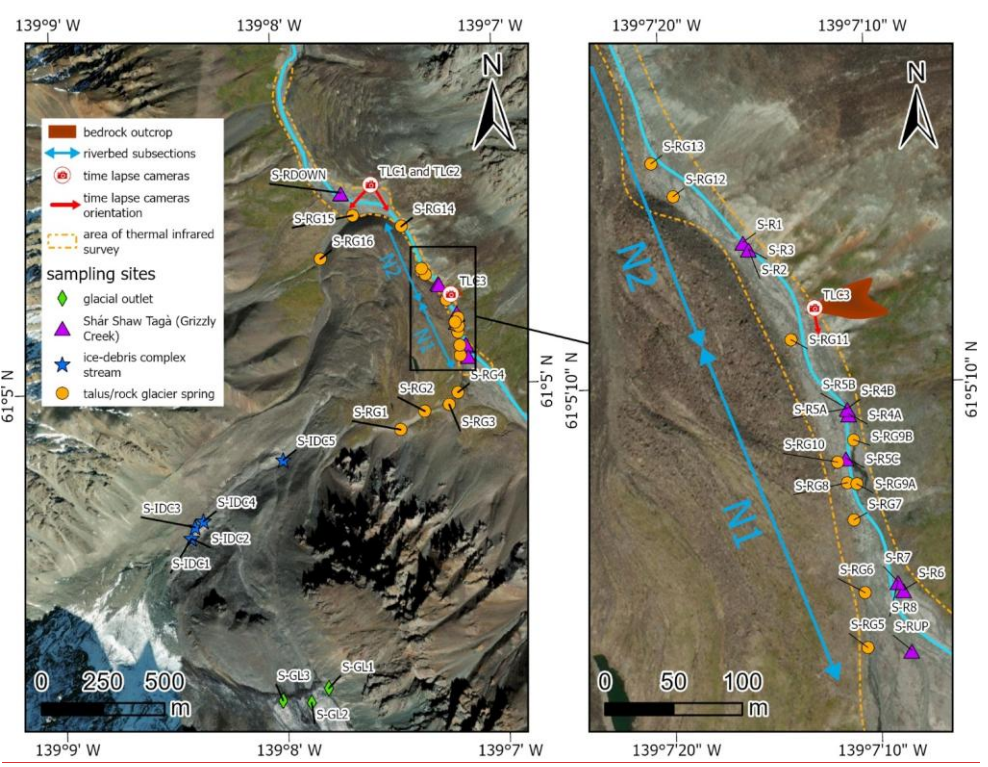


Fig. 2: Map illustrating the methods used in this study Extent of the TIR survey and locations of sampling sites and TL cameras. Panel (a) corresponds to the study area shown in Fig. 1b, while panel (b) provides a zoom-in of panel (a). A bedrock outcrop on the talus slope opposite to RG-AI marks the division of the Shár Shaw Tagà River's "narrow section" into two subsections, NI and N2, as shown on the map. The spring locations represent the outflow points observed during the August 2022 campaign, though their positions may vary depending on hydro-meteorological conditions. Basemap credits: Esri.

#### 4. Results

# 4.1 Monitoring and surveying of groundwater exfiltration

# 4.1.13 TIR survey

The TIR survey identified cold-water emergence zones in the downstream outwash plain and within the N1 subsection of the Shaw Tagà River's "narrow section". Emergence zones from the left bank were labeled TIR-L#, and those from the right bank were labeled TIR-R#. In the imagery, these zones appeared as distinct color contrasts separating warmer surface waters

Formatted: Left

from colder emergences (Fig. 3a). At each site, the mixing plumes were mapped. In the most prominent emergence zones (plumes > 2 m in length), the visible video footage also showed clearer water, which provided additional confirmation of groundwater emergence (Fig. 3b).

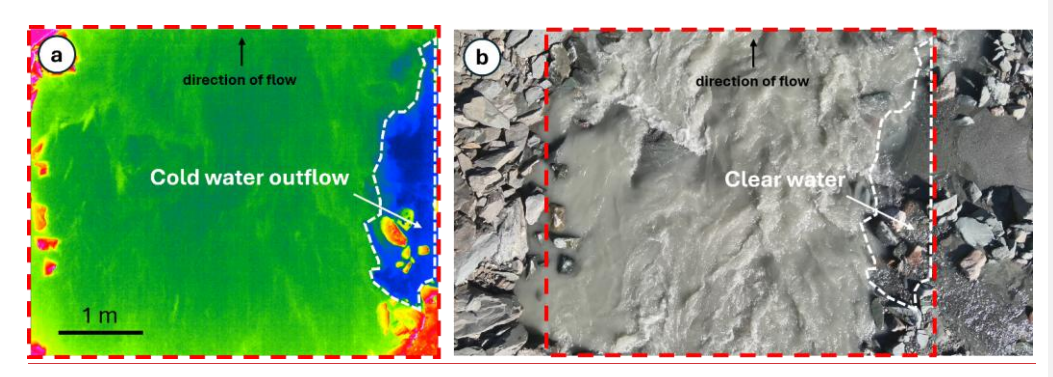


Fig. 3: (a) TIR capture showing cold groundwater emergence (in blue, delimited by the dashed white line), mixing with the warmer waters of the Shár Shaw Tagà River (in green) at the TIR-R2 location. Note that the video does not provide a color scale. (b) RGB image capture showing clear water flowing into the Shár Shaw Tagà River, which is characterized by a significant sediment load at the TIR-R2 location. The cold emergence zone detected with TIR is delimited by the dashed white line. The extent of the TIR capture is indicated by the dashed red line. Flight data and information can be accessed as Supplemental Material in Charonnat and Baraer (2025).

The TIR survey detected four cold emergence zones in the outwash plain downstream of RG-A1 (Fig. 4). Two cold emergence zones were identified on the left bank: one was observed to be associated with meltwater originating from a snow patch at the front of RG-A1, and the other was observed to be from a persistent snow patch on the west flank of the valley. The other two cold emergence zones were located on the right bank, originating from the middle of the outwash plain near the front of RG-B2. These four cold emergence zones are considered not fed by RG-A1, as they originate from snow patches or from the right bank and could not be related to any sampled spring.

Within the "narrow section", eight cold-water emergence zones were identified in the N1 subsection on the left bank of the main channel, and six on the right bank (Fig. 4). No cold-water emergence zone was detected in the N2 subsection. The furthest downstream cold emergence zone in the N1 subsection (TIR-L8) is located just a few meters upstream of the bedrock outcrop. Cold emergence zones on the left bank are generally smaller, with plume lengths ranging from 1 to 6 m, four of these less than 2 m long. In contrast, cold emergence zones on the right bank are larger, with plume lengths ranging from 5 to 14 m, and four exceed 10 m in length.

Of the six cold emergence zones identified on the right bank of the N1 subsection, two were located within a few meters of springs sampled in 2022 and 2023 (TIR-R2 and TIR-R3 can be associated to S-RG9A and S-RG9B, respectively). On the left bank, no cold emergence zone was detected in 2024 directly at the position of springs sampled in 2022 and 2023. However, as noted in Sect. 2, the outflow positions of springs on the left side of the river can shift 10–20 m downstream of the RG-A1 front, depending on river level and meteorological conditions. During the 2024 TIR survey, such conditions prevailed, and cold emergence zones were detected 20 m downstream of springs sampled in 2022 and 2023. Accordingly, cold emergence zones TIR-L1, TIR-L2, and TIR-L8 can be linked to springs S-RG8, S-RG10, and S-RG11, respectively (Fig. 4). The TIR survey detected four cold water outflows outside the "narrow section" of the Shár Shaw Tagà River, located in the outwash plain downstream of RG-A1 (Fig. 9). Two outflows were identified on the left bank: one associated with meltwater originating from a snow patch at the front of RG-A1, and the other is from a persistent snow patch on the west flank of the valley. The other two outflows were located on the right bank, originating from the middle of the outwash plain near the front of RG-B2. These four outflows are not supplied by RG-A1, as they originate from snow patches or from the right bank.

The furthest downstream exfiltration area in the "narrow section" (TIR-L8) is situated in the N1 subsection, just a few meters upstream of the bedrock outcrop (Fig. 9). Within the N1 subsection, eight groundwater exfiltration areas were identified on the left bank of the main channel, and six on the right bank. Exfiltration areas on the left bank are generally smaller, with plume lengths ranging from 1 to 6 m, four of these less than 2 m long. In contrast, exfiltration areas on the right bank are larger, with plume lengths ranging from 5 to 14 m, and four exceed 10 m in length. These exfiltration areas were clearly visible as color contrasts, distinguishing the warmer surface waters from the colder groundwater exfiltrations (Fig. 10a). The positions of the mixing plumes were observed at each location. In the most notable exfiltration areas (plume lengths > 2 m), clearer water was observed in the visible video footage, facilitating the validation of groundwater exfiltration detection (Fig. 10b). Two of the six groundwater exfiltration areas detected from the right bank can be associated with springs sampled and measured during the 2022 and 2023 campaigns for physico-hydrochemical analysis (TIR-R2 and TIR-R3 correspond to S-RG9A and S RG9B, respectively). As mentioned in Sect. 2, depending on the river level and meteorological conditions, the outflow locations of the springs on the left side of the river have been observed to shift 10 to 20 m downstream of the RG-A1 front. During the TIR survey, these conditions were met, and no exfiltration area was found directly at the location of a spring sampled in 2022 and 2023. Instead, exfiltration areas on the left bank were detected 20 m downstream of their corresponding springs sampled earlier. Therefore, exfiltration areas TIR-L1, TIR-L2 and TIR-L8 can be associated with the springs S-RG8, S-RG10 and S-RG11, respectively (Fig. 9).

Overall, tThe drone-based TIR survey identified revealed a high density of cold groundwater exfiltrations water emergence zones along from both the left and right banks of the N1 subsection of the Shár Shaw Tagà River, upstream of the bedrock outcrop. These zones, connected to springs sampled in 2022 and 2023, delineate a significant area of groundwater exfiltration within the upstream half of the "narrow section" of the Shár Shaw Tagà River, where flow is constrained by RG-A1 rock

455

456

457

458

Fig. 49: Location of cold-watercold-water outflows detected by the TIR survey along the Shár Shaw Tagà riverbed. The zoomed-in view of the "narrow section" highlights an area with a high density of cold groundwater outflows detected on both sides of the river, upstream of a bedrock outcrop constraining the riverbed. Additional cold-water outflows are observed in the downstream outwash plain, originated from either snow patch melt on the left side or from the right bank of the outwash plain. Springs that outflow from RG-A1 or the opposite talus slope and were sampled during the 2022 and 2023 campaigns are marked in the zoomed-in panel. Basemap credits: Esri.

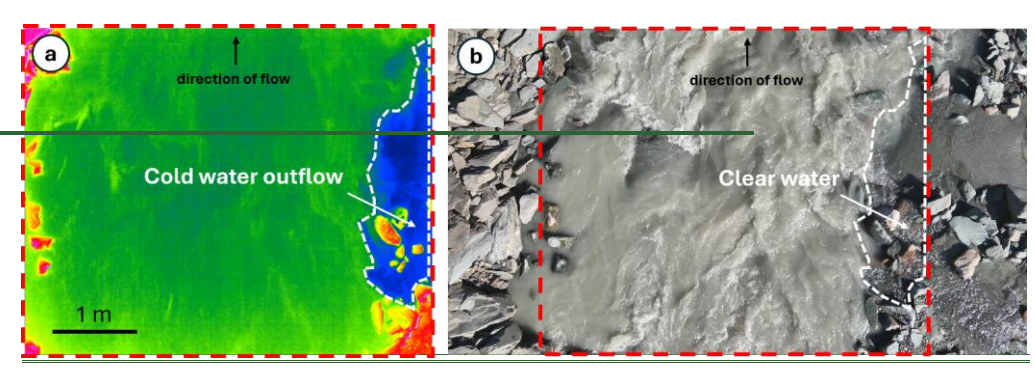


Fig. 10: (a) TIR capture showing cold groundwater outflow (in blue, delimited by the dashed white line), mixing with the warmer waters of the Shár Shaw Tagà River (in green) at the TIR-R2 location. Note that the video does not provide a color scale. (b) RGB image capture showing clear water outflowing into the Shár Shaw Tagà River, which is characterized by a significant sediment load at the TIR-R2 location. The cold water area detected with TIR is delimited by the dashed white line. The extent of the TIR capture is indicated by the dashed red line. Flight data and information can be accessed as Supplemental Material in Charonnat and Baraer, 2025.

4.1.21 TL monitoring

Over theBetween 2018-and-2021 period, TL1 monitored aufeis formation during the winters of 2018-2019 and 2019-2020 (Fig. <u>53 and 4a</u>). No aufeis formation was observed during the winter of 2020-2021. The onset of aufeis development varied between the two winters: Jin 2018-2019, it began in early November and continued to develop throughout the winter season, whereas in 2019-2020, it started in February and progressed through February and March (Fig. <u>53</u>). The development of the aufeis in both winters occurred in phases characterized by multiple flood events. Visible ablation of the aufeis began in May,

Formatted: Normal, Space After: 10 pt, Border: Top: (No border), Bottom: (No border), Left: (No border), Right: (No border), Between: (No border)

with complete melt occurring by June in both 2019 and 2020. The aufeis that formed during the winters of 2018-2019 and 2019-2020 spanned the entire width of the river, from the RG-A1 front to the RG-B2 front.

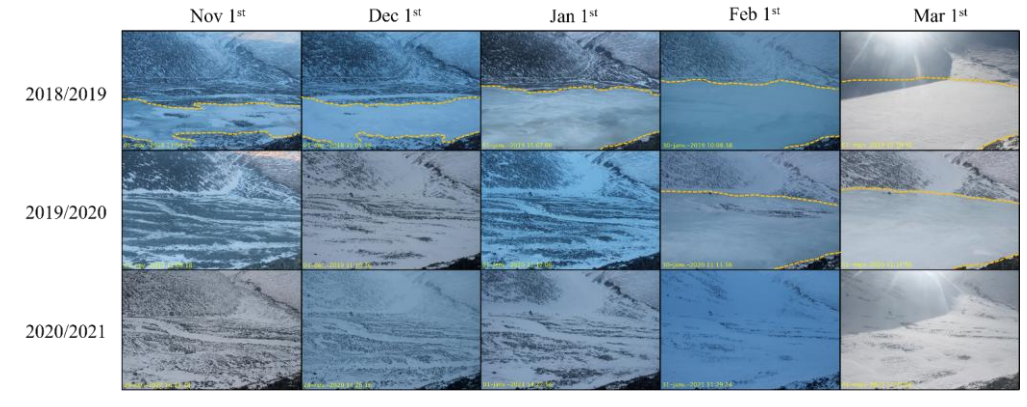


Fig. 53: Monthly timelapse images captured by TL1 of the aufeis from November 1st to March 1st during the winters of 2018-2019, 2019-2020, and 2020-2021. The yellow dashed line indicates the extent of the aufeis in each image when visible. The timelapse images were selected targeting based on the closest date to the first day of each month, with consideration given to image quality. Note that no aufeis formation occurred during the 2020-2021 winter.

TL2, installed in 2019 next to TL1 and oriented towards the aufeis upstream sectionupstream, recorded the formation of the aufeis in the winter of 2019-2020 and its absence during 2020-2021. In the winter of 2020, TL2 captured reflections of liquid water and/or ice at the end of the N2 subsection, when the river was dry (Fig. 6a and 6b4). In subsequent days, the aufeis was observed to form in the downstream outwash plain, starting from the end of the N2 subsection too.

TL3, installed in 2021 to monitor surface outflow in the N1 subsection, showed reflections of liquid water and/or ice from the entrance of the N1 subsection (Fig. 6c), while the upstream outwash plain remained without any visible surface outflow. These is observations indicates uggests that the liquid overflowing water available in winter to supply the aufeis contributing to the formation of the aufeis could originates from the "narrow section" between the upstream and the downstream outwash plains. The only winter during which TLC3 was installed to monitor surface flow in the "narrow section" coincided with the sole winter in which no aufeis developed in the downstream outwash plain. This observation suggests that surface flow in this section may play a more significant role in other years, from the "narrow section" of the Shár Shaw Tagà River.



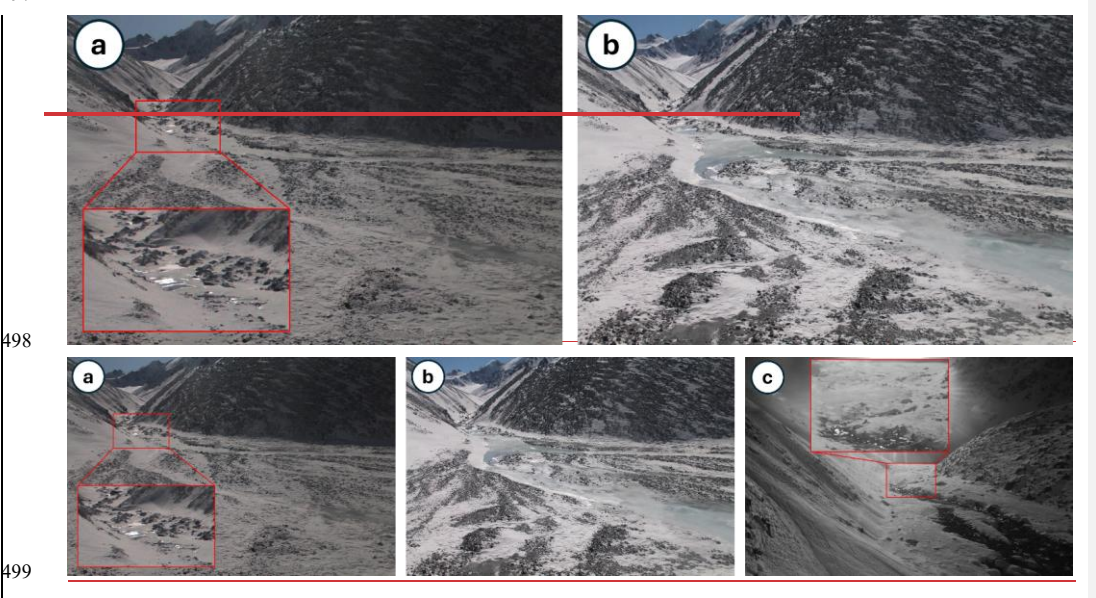


Fig. 64: Initiation of an aufeisWinter outflows in the downstream outwash plain (a, b) and in the N1 subsection (c), captured by TL2 on (a) 04/01/2020 at 08:00, and (b) 08/01/2020 at 11:00, and TL3 on (c) 22/10/2021 at 13:00. The light in the raw images has been enhanced to improve picture quality. (a) and (b) Both images are oriented towards the end of the N2 subsection and the entrance of the downstream outwash plain, while (c) is oriented towards the N1 subsection and the upstream outwash plain in the background. (a) At 8:00 on 04/01/2020, the aufeis has not yet formed, but reflections of ice and/or liquid water are visible at the end of the N2 subsection, during a time when the Shár Shaw Tagà River is dry. (b) At 11:00 on 08/01/2020, the aufeis has started to form in the outwash plain, extending from the end of the N2 subsection. (c) At 13:00 on 22/10/2021, surface outflow is visible from the entrance of the N1 subsection, but no outflow is visible in the upstream outwash plain in the background.

The repetitive monitoring of the aufeis provides evidence of overflow events during late fall and winter, particularly in the 2018-2019 and 2019-2020 periods. The continuous development of aufeis throughout winter, along with its large spatial extent, indicates the presence of a significant and stable water source. The formation of the aufeis is attributed to groundwater outflow from the "narrow section" of the Shár Shaw Tagà River, as the river runs dry in winter in the downstream outwash plain and no aufeis forms in the upstream outwash plain and surface outflow is visible from the N1 subsection. This finding aligns with the high density of springs inventoried along the N1 subsection with the TIR imagery.

## 4.1.3 Radon activities measurements

In June 2023, while the Shár Shaw Tagà River level was lower than in previous years for the same period,  $^{222}$ Rn activities were similar at S-RG8 and S-RG9A, ranging from  $10.17 \times 10^3 \pm 0.22 \times 10^3$  Bq m<sup>-3</sup> to  $10.85 \times 10^3 \pm 0.19 \times 10^3$  Bq m<sup>-3</sup> (Fig. 7). These springs are located along the N1 subsection of the river, at the left and the right of the stream, respectively. In contrast, the Shár Shaw Tagà River at the upstream end of the N1 subsection (S-RUP) exhibited low activities  $(0.36 \times 10^3 \pm 0.06 \times 10^3$  Bq m<sup>-3</sup>), while the downstream end of N1 (S-R1) showed significantly higher activities  $(5.46 \times 10^3 \pm 0.14 \times 10^3$  Bq m<sup>-3</sup>). These results clearly indicate groundwater input to the Shár Shaw Tagà River in the N1 subsection, where S-RG8 and S-RG9A are located.

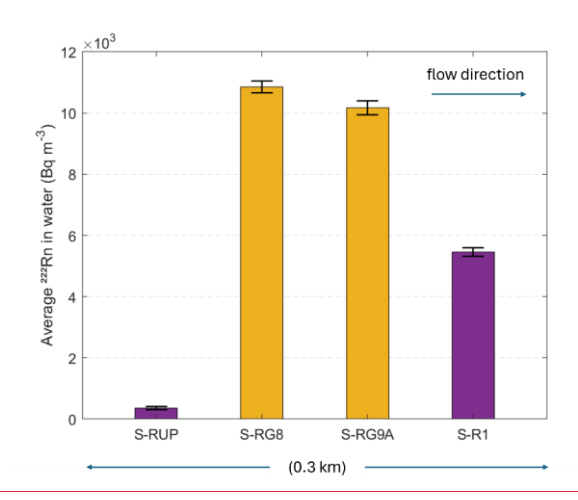


Fig. 7: <sup>222</sup>Rn activities measured with a portable RAD7 Radon Monitor (Durridge) in June 2023. Data were collected at springs S-RG8 and S-RG9A (orange) and along the Shár Shaw Tagà river at upstream (S-RUP) and downstream (S-R1) sites (purple). The bars are arranged from left to right in spatial sequence from upstream to downstream. The error bars represent the uncertainties in the radon activity measurements.

Formatted: Heading 3

Formatted: Font: 9 pt, Bold, Font color: Black

Formatted: Space After: 10 pt, Line spacing: single, Bor Top: (No border), Bottom: (No border), Left: (No border), Right: (No border), Between: (No border)

## 4.2 Physico-hydrochemical characterization

531

532

533

561

562

 $\frac{\text{samples}}{\text{constant}} < 0.13 \text{ mg L}^{-1}$ 

#### 4.2.1 Sampling and field measurements

534 2018 to 2021, and during the 2022 sampling campaigns. This led to a dedicated sampling campaign in June 2023. Many of 535 these springs were sampled across multiple campaigns, indicating their long-term flow. The June 2022 and August 2022 536 sampling campaigns can be directly compared for the springs at RG-A1's front, given their similar spatial coverage and 537 sampling sites. In contrast, the June 2023 sampling campaign focused specifically on the N1 subsection of the river (Table 538 539 The mean water temperature for samples collected from theof springs at RG-A1's frontthe front of RG-A1 in June 2022 was 540 0.90 °C in June 2022, with a range of 3.16 °C, slightly colder than in samples from August 2022 and June 2023, respectively 541 exhibiting a-mean temperatures of 1.38 °C and 1.40 °C and a range of 3.77 °C (Table S1). While cold temperatures The colder 542 conditions in June 2022 may have been strongly influenced bylikely reflect recent snowmelt, no snowwhereas no snow cover 543 remained at the lower elevations of the catchment in during August 2022 and June 2023. In late season, Groundwater outflows 544 with temperatures below 2 °C in late season are commonly interpreted as evidence of adjacent frozen material eold 545 groundwater outflows (<2 °C) suggest the possible presence of frozen content in the vicinity of springs (Carturan et al., 2016; 546 Frauenfelder et al., 1998; Haeberli, 1975; Scapozza, 2009). Accordingly, the cold temperatures measured in August 2022 in 547 the springs at the RG-A1's front inform on persistence of frozen content nearthe front of the rock glacier. 548 The June 2022 campaign recorded a lower mean EC in springs at RG-A1's front of 225.64 µS cm<sup>+</sup>, with a range of 439.10 µS 549 em<sup>-1</sup>, compared to 490.82 µS cm<sup>-1</sup> with a range of 546.72 µS cm<sup>-1</sup> in August 2022. These results indicate dilution due to 550 snowmelt in early season and increased groundwater contribution in late season, consistent with results from other rock glacier 551 hydrology studies (Jones et al., 2019). The hHigh EC ranges (respectively 439.10 µS cm<sup>-1</sup> and 546.72 µS cm<sup>-1</sup> in June and 552 August 2022) highlight underscore the heterogeneous behaviour of the sampled springs. This apparent diversity in physico-553 chemical composition provides the basis for applying PCA to cluster springs according to their properties. Mean pH values 554 were 8.47 in June 2022 and 8.13 in August 2022, with ranges of 1.84 and 1.00, respectively. 555 The mean isotopic composition was more depleted in the springs at RG-A1's front in June 2022 (-23.57 ‰ vs. VSMOW for 556 δ18O and -183.69 ‰ vs. VSMOW for δ2H, with ranges of 1.64 ‰ and 8.78 ‰, respectively) compared to August 2022 (-21.01 557 ‰ vs. VSMOW for δ18O and 169.20 ‰ vs. VSMOW for δ2H, with ranges of 1.38 ‰ and 9.68 ‰, respectively). This depletion 558 is associated with a higher snowmelt contribution in June 2022. Solute concentrations were generally lower in June 2022, 559 frequently falling below detection limits for chlorides (all samples < 0.13 mg L<sup>-1</sup>), potassium (13 out of 20 samples < 0.01 mg 560 L<sup>4</sup>), sodium (13 out of 20 samples < 0.09 mg L<sup>4</sup>), and magnesium (1 out of 20 samples < 0.03 mg L<sup>4</sup>). In contrast, in August

A high concentration of springs was reported along the N1 subsection of the Shár Shaw Tagà River (S-RG5 to S-RG11) from

2022, solute concentrations exceeded detection limits for 38 out of 39 samples for all elements except chlorides (36 out of 39

The June 2023 campaign showed a mean water temperature for the rock glacier springs of 1.40°C, with a range of 0.23 °C. The mean EC value for June 2023 was 678.43  $\mu$ S cm<sup>-1</sup>, with a range of 172.00  $\mu$ S cm<sup>-1</sup>. The mean pH value was 7.82 with a range of 0.23. The mean isotopic composition for the springs during this campaign was -22.86 % vs. VSMOW for  $\delta^{18}$ O and 178.11 % vs. VSMOW for  $\delta^{2}$ H, with ranges of 0.30 % and 1.10 %, respectively.

In June 2023, while the Shár Shaw Tagà River level was lower than in previous years for the same period, <sup>222</sup>Rn activities were similar at S-RG8 and S-RG9A, ranging from 10.17×10<sup>3</sup> ± 0.22×10<sup>3</sup> Bq m<sup>-3</sup> to 10.85×10<sup>3</sup> ± 0.19×10<sup>3</sup> Bq m<sup>-3</sup> (Fig. 5). These springs are located along the N1 subsection of the river, at the left and the right of the stream, respectively. In contrast, the Shár Shaw Tagà River at the upstream end of the N1 subsection (S-RUP) exhibited low activities (0.36×10<sup>3</sup> ± 0.06×10<sup>3</sup> Bq m<sup>-3</sup>), while the downstream end of N1 (S-R1) showed significantly higher activities (5.46×10<sup>3</sup> ± 0.14×10<sup>3</sup> Bq m<sup>-3</sup>). These results indicate a major groundwater input to the Shár Shaw Tagà River in the N1 subsection, where S-RG8 and S-RG9A are located.

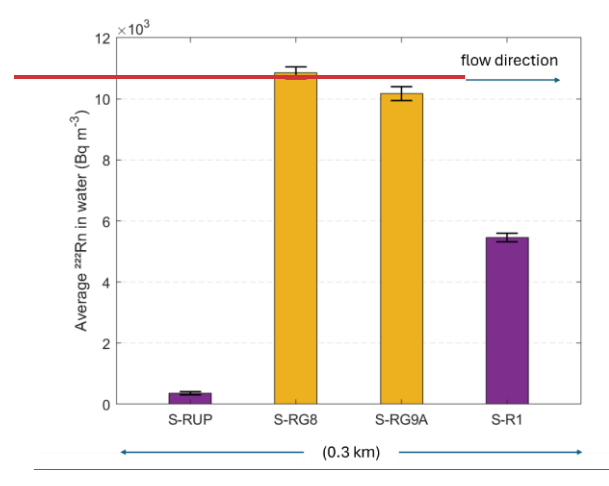


Fig. 5: 222Rn activities measured with a portable RAD7 Radon Monitor (Durridge) in June 2023. Data were collected at springs S-4 RG8 and S-RG9A (orange) and along the Shár Shaw Tagà river at upstream (S-RUP) and downstream (S-R1) sites (purple). The bars are arranged from left to right in spatial sequence from upstream to downstream. The error bars represent the uncertainties in the radon activity measurements.

# 4.2.2 Principal Component Analysis and clustering

#### Samples collected in June 2022

 Principal Component (PC) 1 accounts for 60.96 % of the variance in the dataset and primarily reflects the influence of ionicmineral elements, with PC scores ranging from 0.47 to 0.50 (Fig. 86a). PC2 and PC3, explaining 18.29 % and 14.10 %

**Formatted:** Space After: 0 pt, Line spacing: 1,5 lines, Border: Top: (No border), Bottom: (No border), Left: (No border), Right: (No border), Between: (No border)

Formatted: Font: Not Italic

Formatted: Heading 3, No bullets or numbering

of the variance, respectively, exhibit contrasting associations with the  $\delta^{18}O$  ratio and temperature. PC2 displays a strong positive correlation with the  $\delta^{18}O$  ratio (0.73) and a negative correlation with temperature (-0.67), whereas PC3 shows positive correlations with  $\delta^{18}O$  (0.62) and temperature (0.71).

Clustering analysis based on PCA reveals two distinct clusters among the June 2022 samples (Fig. <u>8</u>6b). Cluster 1 comprises 17 samples characterized by low concentrations of mineral elements (Fig. <u>8</u>6c), with total dissolved solids (TDS) concentrations ranging from 28 to 100 mg L<sup>-1</sup>. In contrast, Cluster 2 includes samples S-RG4, S-RG5, and S-RG8, which show elevated TDS values (90 to 269 mg L<sup>-1</sup>). <u>S-RG5 is grouped within Cluster 2 primarily due to its elevated water temperature, while its other physico-chemical characteristics closely resemble those of the Cluster 1 samples. With the exception of S-RUP, S-RG4, and S-RG15, which record warmer temperatures from 1.43 to 3.19 °C, the remaining 16 samples in the June 2022 dataset exhibit colder temperatures, ranging from 0.03 °C to 0.67 °C (Fig. <u>8</u>6c). The most enriched samples are <u>S-IDC2</u>, S-RG7, S-RG8, and S-RG10, with δ<sup>18</sup>O values between -23 ‰ and -22.6 ‰ vs. VSMOW in δ<sup>18</sup>O (Fig. <u>8</u>6d).</u>

In June 2022, most of the17 springs (Cluster 1)s were supplied by recent snowmelt, as indicated by low concentrations of mineral-mineral elements and cold temperatures. In contrast, S-RG8 and S-RG4 (Cluster 2) were supplied by groundwater, as evidenced by their higher concentrations of mineral elements. The comparatively enriched δ<sup>18</sup>O values of S-IDC2, S-RG7, S-RG8, and S-RG10 may indicate mixing with a source other than snowmelt, such as glacial meltwater, as they approach the δ<sup>18</sup>O values measured in glacial meltwater samples collected in August 2022 (see following paragraph).

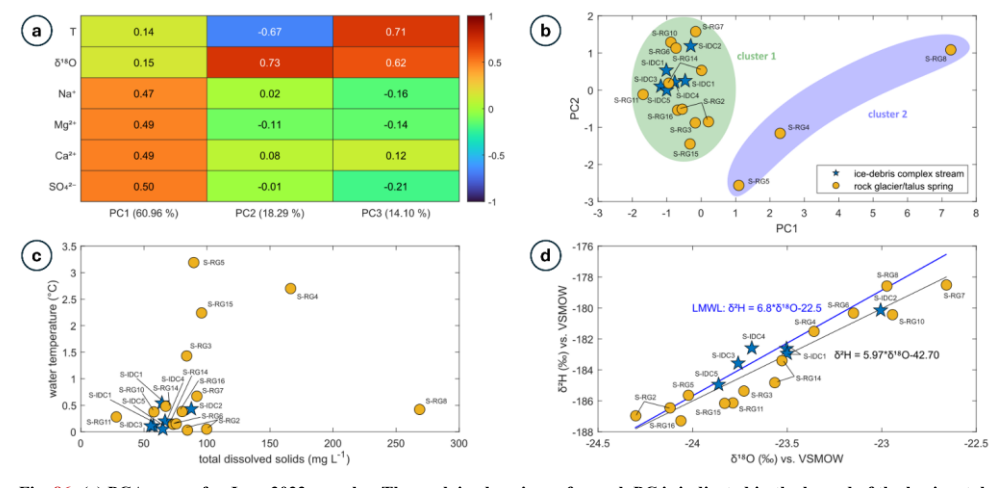


Fig. 86: (a) PCA scores for June 2022 samples. The explained variance for each PC is indicated in the legend of the horizontal axis. (b) Distribution of clusters formed from June 2022 samples following PCA and k-means clustering. Symbols represent different sample types, and ellipses illustrate the distribution of each cluster. (c) Distribution of total dissolved solids (TDS) concentrations and water temperature for the June 2022 samples. (d) Isotopic composition of the June 2022 samples.

# Samples collected in August 2022

605 606

607

608

609

610

611

612

613 614

615

616 617

618

619

620 621

622

623

624

625

626

627

628

629

630

631

632

633

PC1 accounts for 60.57 % of the variance in the dataset and is strongly influenced by solute concentrations, with PC scores ranging from 0.47 to 0.48 (Fig. 97a). PC2, which explains 22.34 % of the variance, reflects opposing influences of temperature (0.68) and isotopic composition (-0.63). PC3, accounting for 9.01 % of the variance, shows joint positive correlations with both temperature (0.71) and isotopic composition (0.63).

Clustering analysis clearly distinguishes different sample types, forming 9 clusters, the maximum achievable based on the parametrization (Fig. 97b). Cluster 3 consists of glacial outlet samples, characterized by low solute concentrations (16 to 38 mg L<sup>-1</sup> in TDS), cold temperatures (0.06 to 0.07 °C), and depleted isotopic compositions (-21.6 to -22 ‰ vs. VSMOW in δ<sup>18</sup>O) as seen in Figs. 97c and 97d. Clusters 5 and 6 comprise Shar Shaw Tagà River samples, with warmer temperatures (3.47 °C to 6.26 °C), higher solute concentrations (88 to 238 mg L<sup>-1</sup> in TDS), and depleted isotopic compositions (-21.8 to -22.2 % vs. VSMOW in  $\delta^{18}$ O). The distinction between these clusters may be attributed to variations in the glacial regime diurnal cycle and weather conditions based on sampling times. Clusters 4 and 8 include samples from springs near the upper end of the rock glacier front and at the transition area with the ice-debris complex (e.g., S-IDC5, S-RG1, S-RG2). As shown in Figs. 97c and 97d, these springs display high concentrations of mineral elements (209 to 304 mg L-1 in TDS) and enriched isotopic compositions (-20.6 to -20.9 ‰ vs. VSMOW in δ18O). Clusters 2 and 9 are represented by springs S-RG7, S-RG8, S-RG9A, and S-IDC1, which exhibit high but narrow ranges of solute concentrations (282 to 309 mg L-1 in TDS) and more depleted isotopic compositions (-21.6 to -21.8 % vs. VSMOW in \delta^{18}O), as shown in Fig. 97d. Clusters 1 and 7 include other springs from the N1 subsection of the Shár Shaw Tagà River, which are characterized by low solute concentrations (111 to 162 mg L-<sup>1</sup> in TDS) and enriched isotopic compositions (-20.4 to -20.9 % vs. VSMOW in  $\delta^{18}$ O). Fig. 97d clearly distinguishes samples with depleted isotopic compositions (below -21.5 % vs. VSMOW in  $\delta^{18}$ O) from those with enriched compositions (above -20.9 ‰ vs. VSMOW in δ18O).

In late summer, the hydrochemical signatures of the springs show significant contrasts, with a high number of clusters. However, springs S-RG7, S-RG8, and S-RG9A share isotopic signatures similar to glacial meltwater from S-G1, S-G2, and S-G3, and Shár Shaw Tagà River samples, indicating a glacial input. Despite being located on opposite sides of the river, these springs cluster together, contrasting with the other springs. 25 Most of the rock glacier spring samples show very cold temperatures (< 2 °C; Fig. 97c). Other springs appear to originate from summer precipitation, as indicated by their enriched isotopic signatures. Among these, some exhibit short residence times, reflected by low solute concentrations (S-RG5, S-RG6, S-RG12, S-RG13, and S-RG14), whereas others show longer residence times, reflected by higher solute concentrations (S-

634 <u>RG1, S-RG2, and S-IDC5).</u>

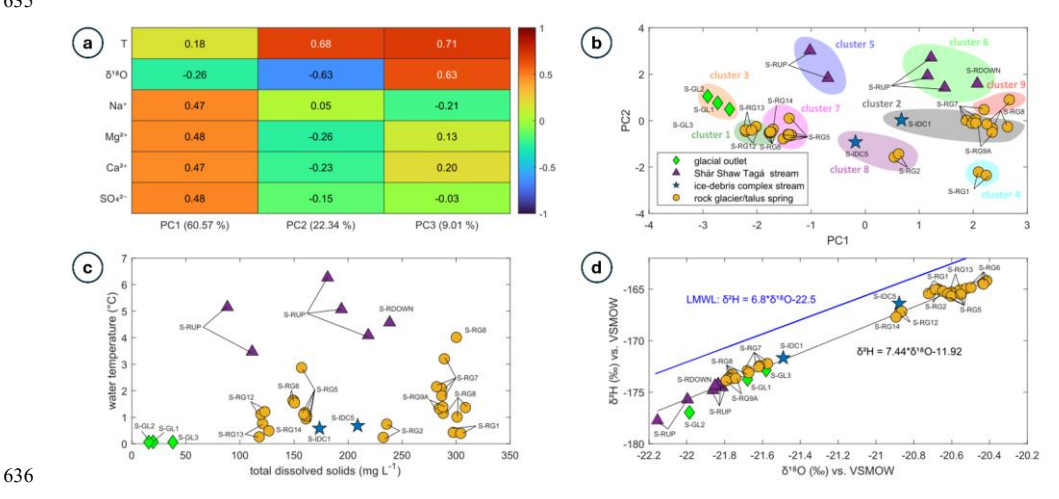


Fig. 27: (a) PCA scores for August 2022 samples. The explained variance for each PC is indicated in the legend of the horizontal axis. (b) Distribution of clusters formed from August 2022 samples following PCA and k-means clustering. Symbols represent different sample types, and ellipses illustrate the distribution of each cluster. (c) Distribution of total dissolved solids (TDS) concentrations and water temperature for the August 2022 samples. (d) Isotopic composition of the August 2022 samples.

# Samples collected in June 2023

PCA conducted on samples collected in June 2023 revealed that PC1 accounts for 68.79 % of the variance (Fig. 108a), primarily driven by solute concentrations (PC scores ranging from 0.40 to 0.48). PC2 and PC3 explain 15.54 % and 10.43 % of the variance, respectively. PC2 is mainly influenced by water temperature (0.88), while PC3 is dominated by isotopic composition (0.86).

The glacier outlet samples form a distinct cluster, labeled as Cluster 3 (Fig. 108b). The remaining samples are divided into two clusters, with a clear distinction based on the maximum number of clusters (5). Cluster 1 consists solely of Shár Shaw Tagà River samples from the upstream part of the N1 subsection. Cluster 2 includes spring samples and Shár Shaw Tagà River samples collected in the downstream part of the N1 subsection. River samples from the downstream N1 subsection and spring samples exhibit higher solute concentrations (from 121 to 147 mg L<sup>-1</sup> in TDS) and colder temperatures (from 0.7 to 4 °C, with 14 out of 16 samples < 2 °C) compared to the upstream N1 samples, which have lower solute concentrations (87 to 125 mg L<sup>-1</sup>) and warmer temperatures (5.3 to 9.5 °C; Fig. 108c). The isotopic composition is generally more enriched for the upstream N1 river samples than for the downstream N1 river and spring samples (Fig. 108d). The isotopic composition of one of the two glacial water samples from G-B1 (sample S-GL1) is similar to the composition from the Shár Shaw Tagà River in upstream N1 (water flowing from G-A1). However, the second S-GL1 sample shows a much more enriched isotopic composition, due

to a two-day interval between the respective samplings. The most enriched sample (-21.2 ‰ vs. VSMOW in  $\delta^{18}O$  and -165.4 ‰ vs. VSMOW in  $\delta^{2}H$ ) was taken first, when the G-B1 glacier was still snow-covered. The most depleted sample (-22.4 ‰ vs. VSMOW in  $\delta^{18}O$  and -173.6 ‰ vs. VSMOW in  $\delta^{2}H$ ) was taken two days later, following significant snowmelt cover on G-B1 and the initiation of glacial melt.

The springs located on opposite sides of the river along the N1 subsection cluster together (Cluster 2) and exhibit close hydrochemical signatures, similar to what was observed in August 2022. By distinguishing between two clusters, the PCA highlights the important influence of these springs on the Shár Shaw Tagà River. Their outflows significantly lower the water temperature and increase solute concentrations in the river.

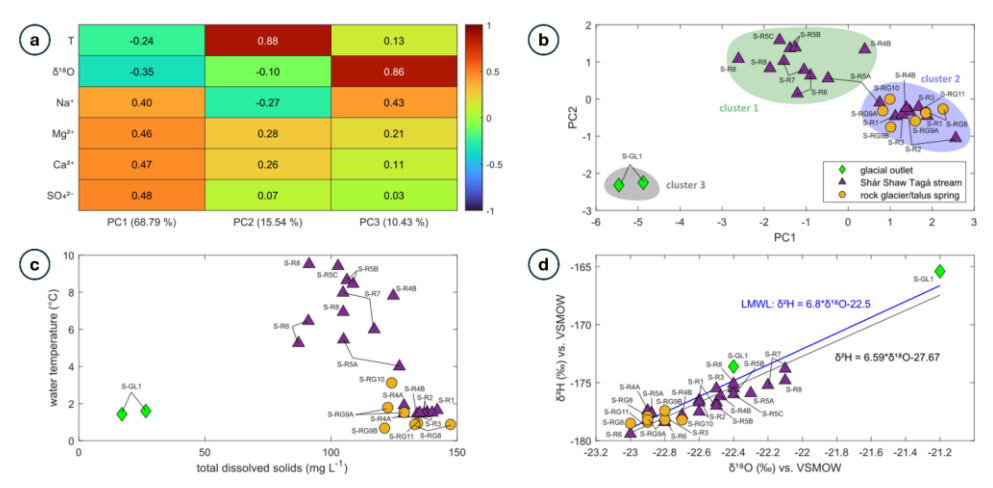


Fig. 108: (a) PCA scores for June 2023 samples. The explained variance for each PC is indicated in the legend of the horizontal axis. (b) Distribution of clusters formed from June 2023 following PCA and k-means clustering. Symbols represent different sample types, and ellipses illustrate the distribution of each cluster. (c) Distribution of total dissolved solids (TDS) concentrations and water temperature for the June 2023 samples. (d) Isotopic composition of the June 2023 samples.

#### Synthesis of physico-hydrochemical characterisation

The springs surrounding RG-A1's front exhibit heterogeneous hydrochemical signatures, highlighting their connection to different drainage systems. However, aA group of springs along the N1 subsection (S-RG7, S-RG8, and S-RG9A) cluster together in PCA and share high EC values, depleted isotopic compositions, high solute concentrations, and similar radon activities. Despite being located on opposite sides of the river, these three springs show striking similarities, suggesting a common origin. Their isotopic compositions are comparable to those of glacial meltwater sampled at the snout of G-B1 and in the Shár Shaw Tagà River, differing significantly from other springs along RG-A1's front. The other springs at theround RG-A1's front exhibit diverse hydrochemical signatures under varying hydro-meteorological conditions. However, they

exhibit signatures of recent precipitation, originating from snowmelt in the early season or rainfall in the late season. Variations in solute concentrations reveal both short and prolonged residence times among these springs, indicating distinct groundwater flow pathways. All Most of the springs consistently exhibit cold temperatures, suggesting flow path adjacent to frozen content. During low-discharge periods, such as June 2023, the springs along the N1 subsection considerably increase downstream solute concentrations and radon activities in the Shár Shaw Tagà River, while their cold outflows reduce stream temperature.

The TIR survey detected four cold water outflows outside the "narrow section" of the Shaw Tagà River, located in the

4.3 TIR survey

678

679

680

681

682

683 684

685

686

687

688

689

690

691

692

693

694

695

696

697

698

699

700

701

702

703

704

705

706

707

708

709

bank, but no groundwater origin was identified for these.

outwash plain downstream of RG-A1 (Fig. 9). Two outflows were identified on the left bank: one associated with meltwater originating from a snow patch at the front of RG-A1, and the other is from a persistent snow patch on the west flank of the valley. The other two outflows were located on the right bank, originating from the middle of the outwash plain near the front of RG-B2. These four outflows are not supplied by RG-A1, as they originate from snow patches or from the right bank. The furthest downstream exfiltration area in the "narrow section" (TIR-L8) is situated in the N1 subsection, just a few meters upstream of the bedrock outcrop (Fig. 9). Within the N1 subsection, eight groundwater exfiltration areas were identified on the left bank of the main channel, and six on the right bank. Exfiltration areas on the left bank are generally smaller, with plume lengths ranging from 1 to 6 m, four of these less than 2 m long. In contrast, exfiltration areas on the right bank are larger, with plume lengths ranging from 5 to 14 m, and four exceed 10 m in length. These exfiltration areas were clearly visible as color contrasts, distinguishing the warmer surface waters from the colder groundwater exfiltrations (Fig. 10a). The positions of the mixing plumes were observed at each location. In the most notable exfiltration areas (plume lengths > 2 m), clearer water was observed in the visible video footage, facilitating the validation of groundwater exfiltration detection (Fig. 10b). Two of the six groundwater exfiltration areas detected from the right bank can be associated with springs sampled and measured during the 2022 and 2023 campaigns for physico-hydrochemical analysis (TIR-R2 and TIR-R3 correspond to S-RG9A and S-RG9B, respectively). As mentioned in Sect. 2, depending on the river level and meteorological conditions, the outflow locations of the springs on the left side of the river have been observed to shift 10 to 20 m downstream of the RG-A1 front. During the TIR survey, these conditions were met, and no exfiltration area was found directly at the location of a spring sampled in 2022 and 2023. Instead, exhiltration areas on the left bank were detected 20 m downstream of their corresponding springs sampled earlier. Therefore, exfiltration areas TIR-L1, TIR-L2 and TIR-L8 can be associated with the springs S-RG8, S-RG10 and S-RG11, respectively (Fig. 9).

Formatted: Normal

The drone-based TIR survey identified a high density of cold groundwater exfiltrations from both the left and right banks of

the N1 subsection of the Shár Shaw Tagà River, upstream of the bedrock outcrop. Exfiltration areas on the right bank exhibited

longer plumes, suggesting higher discharge. Two cold outflows were detected in the downstream outwash plain on the left

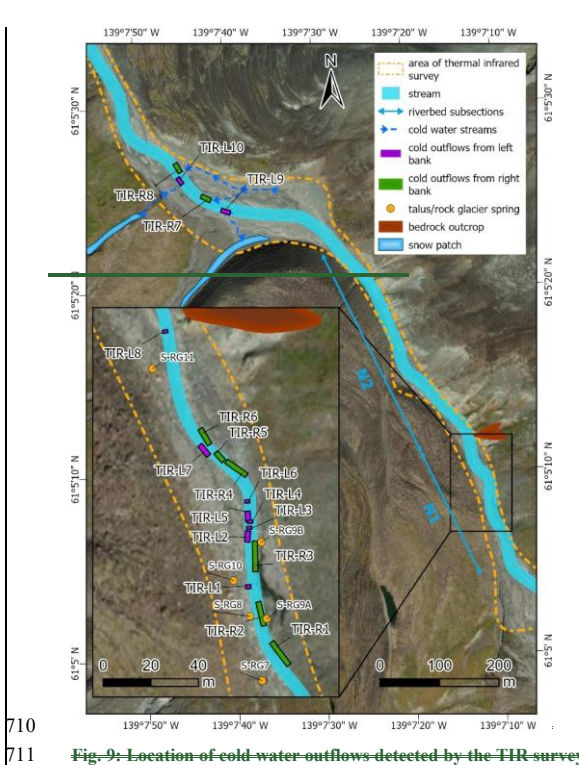


Fig. 9: Location of cold water outflows detected by the TIR survey along the Shar Shaw Tagà riverbed. The zoomed-in view of the "narrow section" highlights an area with a high density of cold groundwater outflows detected on both sides of the river, upstream of a bedrock outerop constraining the riverbed. Additional cold water outflows are observed in the downstream outwash plain, originated from either snow patch melt on the left side or from the right bank of the outwash plain. Springs that outflow from RG-A1 or the opposite talus slope and were sampled during the 2022 and 2023 campaigns are marked in the zoomed-in panel. Basemap credits: Esri.

Formatted: Space After: 0 pt, Line spacing: 1,5 lines

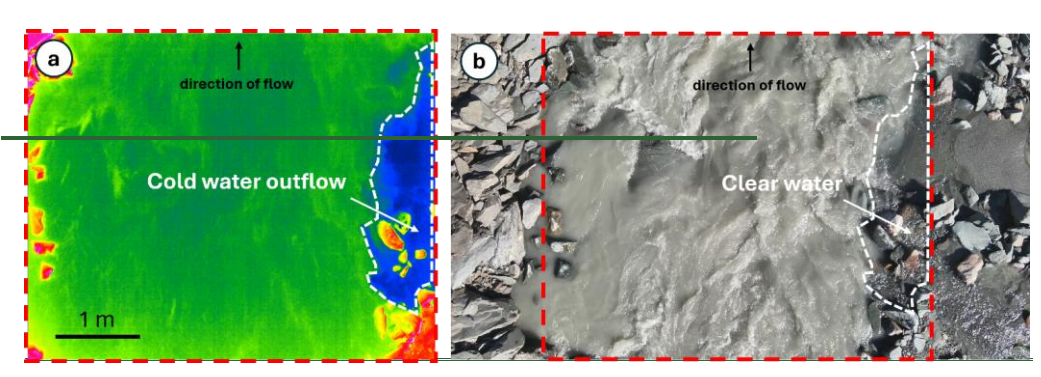


Fig. 10: (a) TIR capture showing cold groundwater outflow (in blue, delimited by the dashed white line), mixing with the warmer waters of the Shár Shaw Tagà River (in green) at the TIR-R2 location. Note that the video does not provide a color scale. (b) RGB image capture showing clear water outflowing into the Shár Shaw Tagà River, which is characterized by a significant sediment load at the TIR-R2 location. The cold water area detected with TIR is delimited by the dashed white line. The extent of the TIR capture is indicated by the dashed red line. Flight data and information can be accessed as Supplemental Material in Charonnat and Baraer, 2025.

Formatted: Space After: 0 pt, Line spacing: 1,5 lines, Border: Top: (No border), Bottom: (No border), Left: (No border), Right: (No border), Between: (No border)

# 5. Discussion ISCUSSION

5.12 Indirect influence of the rock glacier The rock glacier affects downstream cryo-hydrological processes and hydrological continuity

The TIR survey, aufeis monitoring and radon activities measurements identified a major zone of groundwater emergence in the N1 subsection of the Shár Shaw Tagà River, connected to springs both at the front of the rock glacier and on the opposite talus slope. TL camera monitoring confirmed that this zone remains active during winter. Physico-hydrochemical characterization indicates that springs on both banks of the N1 subsection share a glacial meltwater signature. No evidence was found for outflow originating from the head of the rock glacier's subcatchment (fed by glaciers G-B1 and G-B2). Furthermore, contributions from internal ice melt to rock glacier discharge are minimal and exert little influence on isotopic concentrations (Croce and Milana, 2002; Krainer and Mostler, 2002; Krainer et al., 2007).

Thus, these springs do not represent outlets of the rock glacier's internal drainage system. Instead, their similar physicohydrochemical composition indicate the emerging water originates from the same glacial source, which is coherent with field observations. Located on opposite banks of the river, these springs are fed exclusively by upstream outwash plains of the main

Shár Shaw Tagà catchment. In June 2023, surface flow temporarily ceased upstream of the outwash plain, resuming only in the N1 subsection via groundwater inflows. Together, these observations indicate that springs in the N1 subsection are not

740 sourced from the rock glacier, but are rather sustained by a shallow aquifer recharged by upstream glacial meltwater, potentially 741 infiltrating the riverbed or the glacier bed. 742 Parafluvial flow is common in outwash plains with coarse-grained unconsolidated sediments, occurring in river reaches where 743 water is lost before rejoining the river in gaining reaches (Cartwright and Hofmann, 2016). Such plains, often underlain by 744 bedrock, retain groundwater in the shallow subsurface and provide baseflow during low-discharge periods (Müller et al., 2024). 745 In this case, the parafluvial and shallow groundwater resurgence is visible during low-flow periods. The variable location of 746 the springs between sampling campaigns reflects the changes in stored groundwater volume in the alluvial aquifer. The lower 747 density of springs beyond the bedrock outcrop at the downstream end of the N1 subsection suggests a shallow bedrock interface 748 with limited groundwater flow capacity. 749 Cold temperatures in the springs of the N1 subsection indicate that outflows are cooled by adjacent frozen content, such as 750 massive ice or permafrost (e.g. Carturan et al., 2016). Frozen content has been confirmed within the rock glacier by Evin et al. 751 (1997), and is suspected within the talus slope, based on Scapozza (2015). Frozen material on both banks constrains the alluvial 752 aquifer, forcing groundwater to emerge through springs and cold-water upwellings. The narrowing of the riverbed by the 753 advancing rock glacier further enforces this constraint. Consequently, the resurgences in the N1 subsection can be explained 754 by the rock glacier's geomorphic properties: the combination of riverbed narrowing and obstruction by frozen content 755 constrains subsurface flow, demonstrating an indirect hydrological role through geomorphic control. 756 This indirect influence produces a high density of cold springs (<2 °C) along the N1 subsection with distinct physicochemical 757 signatures. The resurgences substantially affect downstream river composition and promote aufeis formation. Solute 758 enrichment in these springs arises from water-rock interactions along groundwater flow paths, with prolonged residence time 759 facilitating the accumulation of dissolved solutes (Hem, 1985). Proximity to buried ground ice and permafrost within the rock 760 glacier and opposite talus slope may further enhance the release of mineral elements through thermal erosion of the ice-761 sediment matrix (Jones et al., 2019). Physico-hydrochemical characterization from June 2023 demonstrates that, during dry 762 periods, these springs notably increase solute concentrations and radon activities, while simultaneously cooling river water. 763 The consequences of the rock glacier's indirect influence are comparable with the direct impact of rock glaciers outflows on 764 the physicochemical characteristics of downstream surface waters, demonstrated in previous studies (e.g., Bearzot et al., 2023; 765 Brighenti et al., 2023; Robinson et al., 2022; Wagner et al., 2021). Yet, our results indicate that rock glaciers can also exert 766 this influence on riverbed systems primarily in an indirect manner, through their geomorphic and thermal properties—a

# 5.2 Direct influence of the rock glacier

mechanism not previously documented in the literature.

767

768

769

770

771

The other springs emerging at the rock glacier front outside the N1 subsection, or within the N1 subsection but not forming a major groundwater emergence area, appear to be associated with the rock glacier's internal drainage system. These springs exhibit limited discharge and exert minimal influence on the riverbed. They are primarily sustained by snowmelt in early

season and by summer precipitation later in the season, with little to no contribution from glacial melt, as indicated by the physico-hydrochemical characterization of samples collected in June 2022 and August 2022. In Canada, precipitation is typically enriched in heavy isotopes during the snow-free period and depleted during winter and spring (Gibson et al., 2020). Accordingly, the depleted isotopic compositions, low solute concentrations, and cold temperatures measured in early June 2022 point to a snowmelt origin, whereas the enriched isotopic compositions in August reflect a stronger rainfall influence. Thus, they are fed by rapid flow paths and respond to meteorological conditions. Variations in solute concentrations among these springs reflect differences in residence time, thereby indicating distinct flow pathways within the rock glacier. Some springs in the N1 subsection likely represent a mix of precipitation-fed and glacier-fed sources, with physicochemical parameters and clustering reflecting these dual contributions depending on hydro-meteorological conditions and timing.

The behaviour and composition of these springs are consistent with observations from other rock glacier hydrology studies (e.g., Jones et al., 2019). Nevertheless, their influence on streamflow discharge and composition appears limited in the immediate vicinity of the rock glacier. Further work beyond the riverbed survey area would be required to locate outflows from the G-B1 and GB-2 subcatchments which could not be detected. The relatively minor impact of these direct outflows contrasts sharply with the substantial indirect influence exerted by resurgences geomorphically constrained by the rock glacier (Sect. 5.1).

The proximity of bedrock and ground ice in the narrow section of the Shár Shaw Tagà River critically reduces the width and depth of the alluvial aquifer, leading to groundwater exfiltrations along the N1 subsection, as discussed in Sect. 5.1. Aufeis typically develop in areas where river flow velocity decreases, such as braided channels and outwash plains (Hu and Pollard, 1997). The TL monitoring suggests that the resurgences from the alluvial aquifer provide the water from the N1 subsection but the decrease in river flow velocity and channel depth creates conditions favourable for the formation of aufeis in the outwash plain immediately downstream of the rock glacier. In contrast, the steeper slope in the N1 subsection likely inhibits aufeis formation directly at the springs locations. Thus, the rock glacier plays a significant role in influencing downstream eryo hydrological processes.

The high density of springs along the N1 subsection and their distinct physicochemical signatures substantially affect the downstream Shár Shaw Tagà River. The solute enrichment observed in these springs is attributed to water rock interactions along groundwater flow paths. Prolonged residence time in aquifers facilitates the accumulation of dissolved solutes (Hems 1985). In addition, the springs may be partially connected to internal drainage systems within the rock glacier, which are known to generate solute rich outflows (Colombo et al., 2018). Lastly, the proximity to buried ground ice and permafrost both within the rock glacier and in adjacent talus slopes—may enhance the release of mineral elements through thermal erosion of the ice-sediment matrix (Jones et al., 2019). The physico-hydrochemical characterization from June 2023 demonstrates that during dry periods, these springs notably increase solute concentrations and radon activities, while simultaneously cooling the river water. These findings are consistent with prior studies showing the influence of rock glaciers on the physicochemical

Formatted: Normal

characteristics of downstream surface waters (e.g., Bearzot et al., 2023; Brighenti et al., 2023; Robinson et al., 2022; Wagner et al., 2021). However, the rock glacier in this study alters the entire riverbed and its physicochemical parameters primarily due to its geomorphic properties. Contrary to initial hypotheses based on early observations and the literature, its internal hydrological behavior does not account for the critical impact the rock glacier has on the riverbed's hydrological system.

5.1 The rock glacier forces resurgence of shallow groundwater flow

The preliminary inventory of springs and the TIR survey identified a high density of spring outflows from both banks of the N1 subsection of the Shár Shaw Tagà River. The physico-hydrochemical characterization indicates that the springs on both

The preliminary inventory of springs and the TIR survey identified a high density of spring outflows from both banks of the NI subsection of the Shár Shaw Tagà River. The physico-hydrochemical characterization indicates that the springs on both banks share a similar signature originating from glacial melt, suggesting a common source (Fig. 7 and 8). The contribution of internal ice melt in rock glacier outflows is known to be minimal and does not significantly influence isotopic signatures (Croce and Milana, 2002; Krainer and Mostler, 2002; Krainer et al., 2007). This evidence supports the conclusion that these springs are fed by groundwater of glacial origin. In June 2023, a low-discharge period, field observations revealed river water losses before entering the upstream outwash plain, where the riverbed temporarily lacked surface flow. Surface flow resumed only from the NI subsection due to groundwater inflows, pointing to the existence of shallow subsurface flow through the upstream outwash plain. Together, these elements indicate that water outflowing from the springs along the NI subsection resurges from lateral shallow groundwater, likely infiltrating through the riverbed and flowing within the lateral alluvial aquifer before resurfacing.

Contrary to initial hypotheses, no evidence was found of outflow originating from the head of the rock glacier's subcatchment (comprising glaciers G-B1 and G-B2). Instead, the physico-hydrochemical characterization suggests that glacial meltwater entering the water to the river derives from upstream outwash plains of the main Shár Shaw Tagà catchment. In contrast, the other springs emerging at the front of the rock glacier appear to be linked to internal drainage systems within the rock glacier itself. These springs are primarily fed by snowmelt in the early season and by summer precipitation later in the season, with minimal or negligible glacier melt contribution, as shown by the physico-hydrochemical characterization of the samples collected in June 2022 and August 2022, respectively. Across Canada, precipitation is typically enriched in heavy isotopes during the snow-free period and depleted during winter and spring (Gibson et al., 2020). Accordingly, the depleted isotopic compositions, low solute concentrations, and cold temperatures measured in early June point to a snowmelt origin, while the enriched isotopic compositions in August reflect a stronger influence from rainfall. This seasonal distinction is further supported by contrasting results from springs in the N1 subsection, which exhibit characteristics of both groundwater and glacier-fed sources. Some springs likely reflect a mix of these sources, with their physicochemical parameters and clustering reflecting these dual influences depending on hydro-meteorological conditions and time periods.

Parafluvial flow is common in outwash plains with coarse-grained unconsolidated sediments, occurring in river reaches where water is lost before rejoining the river in gaining reaches (Cartwright and Hofmann, 2016). Outwash plains, often underlain by bedrock, retaining groundwater in the shallow subsurface, providing baseflow during dry periods when upstream discharge is limited (Müller et al., 2024). Fractured and faulted bedrock aquifers can further contribute to baseflow in outwash plains

Formatted: Normal

(Hayashi, 2019; Müller et al., 2022). In this case, the resurgence of parafluvial and shallow groundwater flow is visible during dry periods. The dynamic location of the springs reported between sampling campaigns reflects the lateral and vertical extent of the alluvial aquifer. The lower density of springs identified beyond the bedrock outcrop at the end of the N1 subsection suggests a shallow bedrock interface with limited groundwater flow capacity. Additionally, the faults inferred along the riverbed in previous geological studies (Dodds and Campbell, 1992) may facilitate groundwater flow from outwash plains upstream of the rock glacier to the N1 subsection, where it is forced to resurge.

The cold temperatures measured in the springs of the N1 subsection indicate that outflows from the alluvial aquifer are cooled by adjacent frozen content, such as massive ice or permafrost (e.g. Carturan et al., 2016). Frozen content has been confirmed in the rock glacier by Evin et al. (1997), and is suspected for the talus slope, based on Seapozza, (2015). The frozen content on both sides of the Shár Shaw Tagà River constrains the alluvial aquifer, forcing groundwater to resurface through springs and cold water upwellings in the riverbed. The advance of the rock glacier, which considerably narrows the riverbed, further enforces this constraint. The younger lobes of the rock glacier, potentially containing higher amounts of frozen content, extend north from the bedrock outcrop to the downstream outwash plain, possibly acting as an additional barrier to groundwater flow where they border the Shár Shaw Tagà River. Thus, the location of the resurgences in the N1 subsection can be explained by the geomorphic properties of the rock glacier. The narrowing of the riverbed by the rock glacier's advance and the presence of frozen content constrain the riverbed, forcing the resurgence of shallow groundwater flow.

#### 5.2 The rock glacier affects downstream cryo-hydrological processes and hydrological continuity

The proximity of bedrock and ground ice in the narrow section of the Shaw Tagà River critically reduces the width and depth of the alluvial aquifer, leading to groundwater exfiltrations along the N1 subsection, as discussed in Sect. 5.1. Aufeis typically develop in areas where river flow velocity decreases, such as braided channels and outwash plains (Hu and Pollard, 1997). The TL monitoring suggests that the resurgences from the alluvial aquifer provide the water from the N1 subsection but the decrease in river flow velocity and channel depth creates conditions favourable for the formation of aufeis in the outwash plain immediately downstream of the rock glacier. In contrast, the steeper slope in the N1 subsection likely inhibits aufeis formation directly at the springs locations. Thus, the rock glacier plays a significant role in influencing downstream error hydrological processes.

The high density of springs along the N1 subsection and their distinct physicochemical signatures substantially affect the downstream Shár Shaw Tagà River. The solute enrichment observed in these springs is attributed to water-rock interactions along groundwater flow paths. Prolonged residence time in aquifers facilitates the accumulation of dissolved solutes (Hem, 1985). In addition, the springs may be partially connected to internal drainage systems within the rock glacier, which are known to generate solute-rich outflows (Colombo et al., 2018). Lastly, the proximity to buried ground ice and permafrost—both within the rock glacier and in adjacent talus slopes—may enhance the release of mineral elements through thermal erosion of the ice-sediment matrix (Jones et al., 2019). The physico-hydrochemical characterization from June 2023 demonstrates that

during dry periods, these springs notably increase solute concentrations and radon activities, while simultaneously cooling the river water. These findings are consistent with prior studies showing the influence of rock glaciers on the physicochemical characteristics of downstream surface waters (e.g., Bearzot et al., 2023; Brighenti et al., 2023; Robinson et al., 2022; Wagner et al., 2021). However, the rock glacier in this study alters the entire riverbed and its physicochemical parameters primarily due to its geomorphic properties. Contrary to initial hypotheses based on early observations and the literature, its internal hydrological behavior does not account for the critical impact the rock glacier has on the riverbed's hydrological system.

## 5.33 Possible Future evolution of the rock glacier influence on catchment hydrology

Predicting the future evolution of the system described in Sect. 5.1 and 5.2 is challenging. Nonetheless However, several scenarios can be envisaged across different timescales ean be envisioned when considering the role of ground ice in constraining the riverbed and driving groundwater resurgences. Frozen content is likely to persist in depositional landforms for an extended periods, as residual ice has been detected in rock glaciers below the modeled elevation limit in multiple cases (e.g., Carturan et al., 2024; Colucci et al., 2019). Future hydrological conditions in alpine catchments will likely be characterized by agre expected to feature a reduced hydrological influence of contribution from glaciers, lower discharge and an an-increased contribution from groundwater and periglacial features to streamflow (Huss et al., 2017; Jones et al., 2019; Zierl and Bugmann, 2005). These conditions were observed during the June 2023 sampling campaign, which occurred took place after the peak of snowmelt and prior to the peak of glacial ablation, leading to resulting in a substantial influence of groundwater resurgences on the Shár Shaw Tagà River. Similar conditions A similar pattern may be expected occur in the future, with groundwater outflows caused by the rock glacier rock glacier-driven groundwater outflows expected to gain influencegaining importance in the Shár Shaw Tagà River.

-However, oHnowever-going cryosphere degradation under rising air temperatures may render this configuration transitory.

Permafrost -thawthe degradation of frozen content within the rock glacier and the opposite talus slopearound the riverbed will likely reduce geomorphic constraints on the riverbed and diminish obstruction of shallow groundwater flow. The dynamic and transient nature of flow paths across the rock glacier has been previously noted (Johnson, 1978). may alter this seenario, as rising air temperatures continue to drive permafrost thaw. AdditionallyFurthermore, thermal and mechanical erosion caused induced by shallowlateral groundwater flow could expand the parafluvial flow zone and create alternative subsurface flow pathspathways, reducing the hydrological discontinuity and disruptive effects currently imposed by of the rock glacier.

The absence of evident streamflow contribution from the G-B1 subcatchment to the Shár Shaw Tagà River, as highlighted in Sect. 5.1, suggests substantial deep infiltration of surface and shallow groundwater flow between the glaciers of the subcatchment and the rock glacier. Although the role of rock glaciers in deep infiltration has not been thoroughly documented to our knowledge, it is suggested that their high vertical and horizontal flow transmissivity may enhance infiltration into deep aquifers and groundwater recharge (Navarro et al., 2023). From a broader perspective, it is considered that deep groundwater systems link mountain cryosphere components to lowlands aquifers through mountain block recharge (van Tiel et al., 2024).

In this context, increased infiltration due to glacial retreat and permafrost degradation may position rock glaciers and other depositional features as critical hubs in proglacial areas, contributing to regional groundwater circulation and water resources.

## 5.44 Limitations and perspectives

The physico-hydrochemical characterization conducted in this study was based on three sampling campaigns conducted under varying hydro-meteorological conditions. These diverse settings posed several challenges for water sampling, including issues with accessibility, safety concerns, periods of no flow, and the need to prioritize specific areas. As a result, some sampling sites could not be revisited during every campaign. Consequently, some sites could not be compared across campaigns, and their characterization can remain incomplete. Leading to gaps in the data over time. Moreover, fluctuating weather conditions during a single campaign in proglacial environments likely contributed to variations in physicochemical parameters at some sites. Whene possible, multiple samples were taken at different times or on different days within the same campaign to minimize biases caused by diurnal and meteorological variations. Consequently, some sites could not be compared across campaigns, and their characterization can remain incomplete. On the other hand, these challenges allowed us to identify the varying influences of different drainage systems on certain springs.

Upon initial observations and hypotheses, we adopted a unique multi-method approach, which evolved as we refined our

Upon initial observations and hypotheses, we adopted a unique multi-method approach, which evolved as we refined our understanding of the system. While this combination of methods was crucial in addressing the research question and drawing the conclusions presented, alternative approaches could have provided a more direct route to the findings. This study demonstrates that the indirect hydrological influence of rock glaciers can exceed their direct influence. Future research could build on these findings insights gained in this study by investigating the hydrological influences of other rock glaciers extending into valley floors to evaluate the representativeness of this case, within the same valley or in different regions. Such studies would help assessclarify whether similar patterns occur across varyingin different settings. Furthermore, monitoring and modelling of comparable configurations could improve predictions of how these systems may evolve and influence catchment hydrology under ongoing cryosphere degradation. Moreover, this research underscores the potential role of the rock glacier and adjacent depositional features in facilitating the infiltration of water into deep groundwater systems, as suggested by the lack of water outflow from the head of the subcatchment to the the Shár Shaw Tagà River. Characterizing these transfers is crucial for understanding the role of proglacial areas in water resource supply during deglaciation. The authors strongly encourage further works in this direction.

## 5 6. Conclusions ONCLUSIONS

The objective of this study was to simultaneously evaluate the direct and indirect influences of a rock glacier on the hydrology of an alpine riverbed. We aim to provide new insights into the hydrological processes and their evolution, focusing on both surface flow and shallow groundwater fluxes within the Shár Shaw Tagà subcatchment, Yukon, Canada.

Formatted: No bullets or numbering

We adopted a multi-method approach combining field observations, drone-based thermal infrared (TIR) surveys, aufeis monitoring and radon activities measurements to identify groundwater emergence zones, alongside physico-hydrochemical analyses of water sources. This methodology enabled us to distinguish contributions originating directly from the rock glacier from those sourced from a shallow aquifer recharged by upstream glacial meltwater.

Our results indicate that the indirect influence of the rock glacier on the riverbed system, through its geomorphic and thermal properties constraining subsurface flow, exerts a greater impact on discharge and water chemistry than direct contributions from the rock glacier. The dynamic landform functions as a structural constraint within the riverbed, forcing groundwater resurgence and substantially affecting downstream physicochemical properties and aufeis formation.

The presence of frozen content in the rock glacier and in the opposite talus slope is central to this indirect influence, modulating constraint on the alluvial aquifer and likely governing the evolution of these flows under ongoing deglaciation and permafrost thaw. Understanding this factor is therefore essential for anticipating changes in alpine hydrological systems under climate warming.

Our findings highlight that studies of rock glacier hydrology on catchments should account for indirect effects, which can surpass direct contributions and play a critical role in redistributing both surface and subsurface waters in alpine environments.

The geomorphic properties of rock glaciers make them dynamic features capable of altering riverbed hydrological systems. As assessed in this study, rock glaciers can obstruct proglacial outwash plains, thereby controlling and constraining shallow groundwater flow. This obstruction results in channel confinement, which induces resurgences from the alluvial aquifer, with profound impacts on both the hydrochemistry and hydrogeomorphology of alpine catchments. Rock glacier disruption leads to substantial changes in the physicochemical parameters of streamflow, and contributes to the formation of aufeis, a consequence not previously documented in the literature. In contrast to initial hypotheses, the internal hydrological system of the rock glacier does not exhibit a significant influence on downstream surface waters. Instead, the critical disruption to the riverbed hydrological system is due to the geomorphic constraint imposed by the rock glacier on the alluvial aquifer. The water that flows from the subcatchment above the rock glacier is suspected to infiltrate deep groundwater systems through the rock glacier and the adjacent depositional features, as it could not be traced beyond the rock glacier. Thus, this study emphasizes the complexity and potentially misleading nature of characterizing groundwater flow pathways in proglacial environments. The findings also have broader implications for mountain hydrology and water resources, highlighting the importance of rock glaciers and proglacial systems as critical hydrological features and potential hubs for mountain block recharge, linking the mountain cryosphere to deep groundwater systems.

# Appendix: Table A1

		Dates and times of sampling

(UTM) 6773938 6773933 6773933	(UTM) 601332 601336	(m a.s.l.) 1738	Shár Shaw Tagà river (narrow section)	NV	NV	15/06/23 12:50
6773933	601336		section)	NV	NV	15/06/23 12:50
		1739	,			
		1739	Cl. (- Cl T )	1	İ	16/06/23 13:00
6773933			Shár Shaw Tagà river (narrow	NV	NV	15/06/23 13:07
6773933			section)			16/06/23 13:10
	601336	1739	Shár Shaw Tagà river (narrow	NV	NV	15/06/23 13:25
			section)			16/06/23 13:40
6773813	601409	1741	Shár Shaw Tagà river (narrow	NV	NV	15/06/23 13:50
			section)			
6773817	601408	1746	Shár Shaw Tagà river (narrow	NV	NV	15/06/23 14:35
			section)			16/06/23 14:20
6773817	601408	1746	Shár Shaw Tagà river (narrow	NV	NV	15/06/23 14:40
			section)			16/06/23 15:10
6773817	601408	1746	Shár Shaw Tagà river (narrow	NV	NV	15/06/23 14:10
			section)			16/06/23 15:25
6773781	601407	1747	Shár Shaw Tagà river (narrow	NV	NV	16/06/23 14:45
			section)			
6773685	601449	1759	Shár Shaw Tagà river (narrow	NV	NV	15/06/23 16:40
			section)			16/06/23 15:45
6773691	601445	1753	Shár Shaw Tagà river (narrow	NV	NV	15/06/23 16:50
			section)			16/06/23 16:00
6773691	601445	1753	Shár Shaw Tagà river (narrow	NV	NV	15/06/23 17:00
			section)			16/06/23 16:10
6774302	600936	1687	Shár Shaw Tagà river (downstream	NV	19/08/22 13:05	NV
			floodplain)			
6773641	601455	1749	Shár Shaw Tagà river (upstream	NV	16/08/22 12:00	NV
			floodplain)		16/08/22 16:16	
					17/08/22 13:12	
					18/08/22 12:35	
6772289	600889	2083	stream at G-B1 snout	NV	18/08/22 18:36	19/06/23 14:35
						21/06/23 12:05
6772230	600819	2109	stream at G-B1 snout	NV	18/08/22 18:06	NV
6772239	600703	2086	stream at G-B1 snout	NV	18/08/22 19:03	NV
6	5773817 5773817 5773781 5773781 5773685 5773691 5773691 5773641 5773641	5773817 601408 5773817 601408 5773781 601407 5773685 601449 5773691 601445 5773691 601445 5774302 600936 5774302 600936 5772289 600889	5773817         601408         1746           5773817         601408         1746           5773781         601407         1747           5773685         601449         1759           5773691         601445         1753           5773691         601445         1753           5773691         601445         1753           5773691         601445         1749           5773641         601455         1749           5772289         600889         2083           5772230         600819         2109	Section   Shár Shaw Tagà river (narrow section   Shár Shaw Tagà river (downstream floodplain   Shár Shaw Tagà river (upstream floodplain   Shár Shaw Tagà river (up	Section   Sect	5773817         601408         1746         Shár Shaw Tagà river (narrow section)         NV         NV           5773817         601408         1746         Shár Shaw Tagà river (narrow section)         NV         NV           5773817         601408         1746         Shár Shaw Tagà river (narrow section)         NV         NV           5773781         601407         1747         Shár Shaw Tagà river (narrow section)         NV         NV           5773685         601449         1759         Shár Shaw Tagà river (narrow section)         NV         NV           5773691         601445         1753         Shár Shaw Tagà river (narrow section)         NV         NV           5773691         601445         1753         Shár Shaw Tagà river (narrow section)         NV         NV           5774302         600936         1687         Shár Shaw Tagà river (downstream floodplain)         NV         19/08/22 13:05           5773641         601455         1749         Shár Shaw Tagà river (upstream floodplain)         NV         16/08/22 16:16           5772289         600889         2083         stream at G-B1 snout         NV         18/08/22 18:06           5772230         600819         2109         stream at G-B1 snout         NV         18/08/22 18:0

S-IDC1	6772896	600330	1886	ice-debris complex stream	16/06/22 15:56	18/08/22 20:29	NV
					18/06/22 17:50		
S-IDC2	6772897	600330	1886	ice-debris complex stream	18/06/22 17:56	NV	NV
S-IDC3	6772943	600345	1891	ice-debris complex stream	16/06/22 15:37	NV	NV
S-IDC4	6772967	600379	1893	ice-debris complex stream	16/06/22 17:04	NV	NV
S-IDC5	6773216	600703	1860	ice-debris complex stream	16/06/22 17:40	18/08/22 20:55	NV
S-RG1	6773340	601180	1797	spring at RG-A1 front	NV	17/08/22 11:58	NV
S-KG1	0//3340	001180	1/9/	spring at KG-A1 from	INV	18/08/22 11:58	IN V
S-RG2	6773415	601279	1780	spring at RG-A1 front	12/06/22 16:54	16/08/22 11:15	NF
					19/06/22 15:08	17/08/22 12:14	
S-RG3	6773442	601378	1770	spring at RG-A1 front	19/06/22 14:48	NF	NF
S-RG4	6773492	601414	1770	spring at RG-A1 front	19/06/22 13:52	NF	NF
S-RG5	6773643	601423	1770	spring at RG-A1 front	19/06/22 13:45	16/08/22 11:30	NV
						16/08/22 16:04	
						17/08/22 12:44	
						18/08/22 12:47	
						19/08/22 13:46	
S-RG6	6773683	601421	1758	spring at RG-A1 front	19/06/22 13:30	16/08/22 12:40	NV
						17/08/22 13:05	
						18/08/22 12:27	
						19/08/22 13:24	
S-RG7	6773736	601413	1746	spring at RG-A1 front	19/06/22 13:18	16/08/22 13:05	NV
						17/08/22 13:58	
						18/08/22 12:14	
						19/08/22 13:12	
S-RG8	6773763	601408	1744	spring at RG-A1 front	19/06/22 12:50	16/08/22 13:15	15/06/23 14:55
				-		17/08/22 14:13	16/06/23 14:35
						18/08/22 11:11	
						19/08/22 12:34	
S-RG9A	6773762	601415	1752	spring flowing from talus opposite	NV	16/08/22 12:13	15/06/23 14:55
				to RG-A1 front (right bank)		17/08/22 13:29	16/06/23 14:25
S-RG9B	6773931	601335	1734	spring from talus opposite to RG-	NV	NV	16/06/23 14:10
				A1 front (right bank)			

S-RG10	6773778	601401	1749	spring at RG-A1 front	19/06/22 12:43	NV	16/06/23 14:00
S-RG11	6773867	601367	1738	spring at RG-A1 front	19/06/22 12:35	NV	16/06/23 13:30
S-RG12	6773971	601281	1726	spring at RG-A1 front	NV	18/08/22 11:56 19/08/22 12:10	NV
S-RG13	6773995	601265	1726	spring at RG-A1 front	NV	16/08/22 13:47 18/08/22 11:40	NV
S-RG14	6774166	601183	1712	spring at RG-A1 front	15/06/22 15:30 19/06/22 14:25	19/08/22 12:30	NV
S-RG15	6774210	600985	1683	spring at RG-A1 front	19/06/22 15:17	NV	NV
S-RG16	6774034	600854	1740	spring at RG-A1 front	19/06/22 15:42	NV	NV

Table A1: List and description of sites sampled during the three campaigns between June 2022 and August 2023, with UTM coordinates, elevation, dates and times of sampling. Samples are categorized into four distinct types: glacial outlets from the G-B1 glacier snout (S-GL#), ice-debris complex streams in the proglacial area between the glacier tongue and rock glaciers (S-IDC#), Shár Shaw Tagà River (S-R#), and springs from RG-A1 rock glacier front and opposite talus (S-RG#). Sites were not all sampled for every campaign, due to diverse reasons (access and safety issues, no flow, campaign dedicated to a specific area, etc.). When possible, sites were sampled several times to trace potential fluctuations in their physico-chemical signature. When not sampled, the comment "NV" stands for "not visited." The comment "NF," for "no flow," indicates a site not sampled as it was dry when visited.

## Code/Data availability

 The data supporting this study are available upon request to the corresponding author.

# Video supplement

The videos and flight data used for the TIR analysis are available as Supplemental Material in Charonnat and Baraer, 2025, on Borealis dataverse ( <a href="https://doi.org/10.5683/SP3/O57OMY">https://doi.org/10.5683/SP3/O57OMY</a>).

#### Author contribution

Conceptualization: B.C. and M.B. Data curation: B.C. Formal analysis: B.C., M.B., J.M.-D. and C.M. Funding acquisition: M.B. and J.M.M. Investigation: B.C., M.B., E.V., J.M.-D., K.W. and E.D. Methodology: B.C., M.B., E.V. and J.M.-D. Project administration: B.C., M.B., E.V. and J.M.-D. Supervision: M.B., J.M.-D. and J.M.M. Visualization: B.C. and K.W. Writing – original draft preparation: B.C. Writing – review & editing: B.C., M.B., E.V., J.M.-D., C.M., K.W., E.D. and J.M.M. All authors have read and agreed to the published version of the manuscript.

## Competing interests

The authors declare that they have no conflict of interest.

#### Acknowledgements

988

989

994 995

998

1000

- 990 We are grateful to the Kluane First Nation and the White River First Nation for the opportunity to conduct research on their
- 991 territory. We thank the Arctic Institute of North America and the University of Calgary for providing us service and access to
- 992 their facilities at Kluane Lake Research Station. We thank Parks Canada for their collaboration and for issuing permits that
- 993 allowed us to conduct research within Kluane National Park and Reserve.

#### Financial support

- 996 This research was supported by the Natural Sciences and Engineering Research Council of Canada, grant numbers RGPIN-
- 997 2020-05612 and RGPNS-2020-05612, and by Natural Resources Canada—Polar Continental Shelf Program, grant number
  - 62723. Additional funding for the expedition was provided by the Research Centre on the Dynamics of the Earth System
- 999 (GEOTOP).

#### References

- 1001 Abolt, C., Caldwell, T., Wolaver, B., and Pai, H.: Unmanned aerial vehicle-based monitoring of groundwater inputs to surface
- waters using an economical thermal infrared camera, Optical Engineering, 57(05), 1, https://doi.org/10.1117/1.oe.57.5.053113,
- 1003 2018.
- 1004 Antonelli, M., Klaus, J., Smettem, K., Teuling, A. J., and Pfister, L.: Exploring Streamwater Mixing Dynamics via Handheld
- 1005 Thermal Infrared Imagery, Water, 9(5), Article 5, <a href="https://doi.org/10.3390/w9050358">https://doi.org/10.3390/w9050358</a>, 2017.
- 1006 Arenson, L. U., Harrington, J. S., Koenig, C. E. M., and Wainstein, P. A.: Mountain Permafrost Hydrology—A Practical
- 1007 Review Following Studies from the Andes, Geosciences, 12(2), Article 2, https://doi.org/10.3390/geosciences12020048, 2022.
- 1008 Arenson, L., Hoelzle, M., and Springman, S.: Borehole Deformation Measurements and Internal Structure of Some Rock
- 1009 Glaciers in Switzerland, Permafrost and Periglacial Processes, 13, 117-135, https://doi.org/10.1002/ppp.414, 2002.
- 1010 Baker, E. A., Lautz, L. K., Kelleher, C. A., and McKenzie, J. M.: The importance of incorporating diurnally fluctuating stream
- 1011 discharge in stream temperature energy balance models, Hydrological Processes, 32(18), 2901-2914,
- 1012 <a href="https://doi.org/10.1002/hyp.13226">https://doi.org/10.1002/hyp.13226</a>, 2018.
- 1013 Baraer, M., McKenzie, J., Bury, J., and Knox, S.: Characterizing contributions of glacier melt and groundwater during the dry
- 1014 season in a poorly gauged catchment of the Cordillera Blanca (Peru), Advances in Geosciences, 22, 41-49,
- 1015 https://doi.org/10.5194/adgeo-22-41-2009, 2009.

- 1016 Baraer, M., McKenzie, J., Mark, B. G., Gordon, R., Bury, J., Condom, T., Gomez, J., Knox, S., and Fortner, S. K.: Contribution
- 1017 of groundwater to the outflow from ungauged glacierized catchments: A multi-site study in the tropical Cordillera Blanca,
- 1018 Peru, Hydrological Processes, 29(11), Article 11, <a href="https://doi.org/10.1002/hyp.10386">https://doi.org/10.1002/hyp.10386</a>, 2015.
- 1019 Barclay, J. R., Briggs, M. A., Moore, E. M., Starn, J. J., Hanson, A. E. H., and Helton, A. M.: Where groundwater seeps:
  - Evaluating modeled groundwater discharge patterns with thermal infrared surveys at the river-network scale, Advances in
- Water Resources, 160, 104108, https://doi.org/10.1016/j.advwatres.2021.104108, 2022.
- 1022 Barsch, D.: Rockglaciers: Indicators for the present and former geoecology in high mountain environments, 1996.
- 1023 Bearzot, F., Colombo, N., Cremonese, E., di Cella, U. M., Drigo, E., Caschetto, M., Basiricò, S., Crosta, G. B., Frattini, P.,
- 1024 Freppaz, M., Pogliotti, P., Salerno, F., Brunier, A., and Rossini, M.: Hydrological, thermal and chemical influence of an intact
- 1025 rock glacier discharge on mountain stream water, Science of The Total Environment, 876, 162777,
- 1026 https://doi.org/10.1016/j.scitotenv.2023.162777, 2023.

- 1027 Birks, S. J., Edwards, T. W. D., Gibson, J. J., Drimmie, R. J. and Michel, F. A.: Canadian network for isotopes in Precipitation,
- 1028 http://www.science.uwaterloo.ca/~twdedwar/cnip/cniphome.html, 2004.
- 1029 Blöthe, J. H., Rosenwinkel, S., Höser, T., and Korup, O.: Rock-glacier dams in High Asia, Earth Surface Processes and
- Landforms, 44(3), 808–824, https://doi.org/10.1002/esp.4532, 2019.
- 1031 Bodin, X., Schoeneich, P., Deline, P., Ravanel, L., Magnin, F., Krysiecki, J.-M., and Echelard, T.: Le permafrost de montagne
- 1032 et les processus géomorphologiques associés: Évolutions récentes dans les Alpes françaises, Journal of Alpine Research
- 1033 Revue de géographie alpine, 103–2, https://doi.org/10.4000/rga.2806, 2015.
- 1034 Bolch, T., and Marchenko, S.: Significance of glaciers, rockglaciers and ice-rich permafrost in the Northern Tien Shan as water
- towers under climate change conditions, IHP/HWRP-Berichte, 8, Article 8, https://doi.org/10.5167/uzh-137250, 2009.
- 1036 Brahney, J., Clague, J. J., Edwards, T. W. D., and Menounos, B.: Late Holocene paleohydrology of Kluane Lake, Yukon
- 1037 Territory, Canada, Journal of Paleolimnology, 44(3), 873 885, https://doi.org/10.1007/s10933-010-9459-8, 2010.
- 1038 Briggs, M. A., Hare, D. K., Boutt, D. F., Davenport, G., and Lane, J. W.: Thermal infrared video details multiscale groundwater
- 1039 discharge to surface water through macropores and peat pipes, Hydrological Processes, 30(14), 2510-2511,
- 1040 https://doi.org/10.1002/hyp.10722, 2016.
- 1041 Brighenti, S., Engel, M., Dinale, R., Tirler, W., Voto, G., and Comiti, F.: Isotopic and chemical signatures of high mountain
- 1042 rivers in catchments with contrasting glacier and rock glacier cover, Journal of Hydrology, 623,
- 1043 https://doi.org/10.1016/j.jhydrol.2023.129779, 2023.
- 1044 Brighenti, S., Tolotti, M., Bruno, M. C., Engel, M., Wharton, G., Cerasino, L., Mair, V., and Bertoldi, W.: After the peak
- 1045 water: The increasing influence of rock glaciers on alpine river systems, Hydrological Processes, 33(21), 2804-2823,
- 1046 https://doi.org/10.1002/hyp.13533, 2019.
- 1047 Brunner, P., Therrien, R., Renard, P., Simmons, C. T., and Franssen, H.-J. H.: Advances in understanding river-groundwater
- 1048 interactions, Reviews of Geophysics, 55(3), 818–854, <a href="https://doi.org/10.1002/2017RG000556">https://doi.org/10.1002/2017RG000556</a>, 2017.

## Field Code Changed

- 1049 Carrivick, J. L., and Heckmann, T.: Short-term geomorphological evolution of proglacial systems, Geomorphology, 287, 3-
- 28, https://doi.org/10.1016/j.geomorph.2017.01.037, 2017.
- 1051 Carturan, L., Zuecco, G., Andreotti, A., Boaga, J., Morino, C., Pavoni, M., Seppi, R., Tolotti, M., Zanoner, T., and Zumiani,
- 1052 M.: Spring-water temperature suggests widespread occurrence of Alpine permafrost in pseudo-relict rock glaciers, EGUsphere,
  - 1-35, https://doi.org/10.5194/egusphere-2023-2689, 2024.
- 1054 Cartwright, I., and Hofmann, H.: Using radon to understand parafluvial flows and the changing locations of groundwater
- 1055 inflows in the Avon River, southeast Australia, Hydrology and Earth System Sciences, 20(9), 3581-3600,
- 1056 https://doi.org/10.5194/hess-20-3581-2016, 2016.
- 1057 Casas-Mulet, R., Pander, J., Ryu, D., Stewardson, M. J., and Geist, J.: Unmanned Aerial Vehicle (UAV)-Based Thermal Infra-
- 1058 Red (TIR) and Optical Imagery Reveals Multi-Spatial Scale Controls of Cold-Water Areas Over a Groundwater-Dominated
- Riverscape, Frontiers in Environmental Science, 8, https://doi.org/10.3389/fenvs.2020.00064, 2020.
- 1060 Chakravarti, P., Jain, V., and Mishra, V.: The distribution and hydrological significance of intact rock glaciers in the north
  - west Himalaya, Geografiska Annaler, Series A: Physical Geography, 104(3), 226-244,
- 1062 https://doi.org/10.1080/04353676.2022.2120262, 2022.
- 1063 Charonnat, B. and Baraer, M.: Supplemental Material: Drone-Based Thermal Infrared Imagery for Detection of Cold
- 1064 Groundwater Exfiltration in Shár Shaw Tagà, Yukon, Canada, Borealis, V1, https://doi.org/10.5683/SP3/O57OMY, 2025.
- 1065 Chesnokova, A., Baraer, M., and Bouchard, É.: Proglacial icings as records of winter hydrological processes, The Cryosphere,
- 1066 14(11), 4145–4164, https://doi.org/10.5194/tc-14-4145-2020, 2020.
- 1067 Clow, D. W., Striegl, R. G., and Dornblaser, M. M.: Spatiotemporal Dynamics of CO2 Gas Exchange From Headwater
- 1068 Mountain Streams, Journal of Geophysical Research: Biogeosciences, 126(9), https://doi.org/10.1029/2021JG006509, 2021.
- 1069 Colombo, N., Ferronato, C., Vittori Antisari, L., Marziali, L., Salerno, F., Fratianni, S., D'Amico, M. E., Ribolini, A., Godone,
- 1070 D., Sartini, S., Paro, L., Morra di Cella, U., and Freppaz, M.: A rock-glacier pond system (NW Italian Alps): Soil and
- 1071 sediment properties, geochemistry, and trace-metal bioavailability, Catena, 194, https://doi.org/10.1016/j.catena.2020.104700,
- 1072 2020.

1053

- 1073 Colombo, N., Gruber, S., Martin, M., Malandrino, M., Magnani, A., Godone, D., Freppaz, M., Fratianni, S., and Salerno, F.:
- 1074 Rainfall as primary driver of discharge and solute export from rock glaciers: The Col d'Olen Rock Glacier in the NW Italian
- 1075 Alps, Science of the Total Environment, 639, 316–330, https://doi.org/10.1016/j.scitotenv.2018.05.098, 2018.
- 1076 Colombo, N., Salerno, F., Martin, M., Malandrino, M., Giardino, M., Serra, E., Godone, D., Said-Pullicino, D., Fratianni, S.,
  - Paro, L., Tartari, G., and Freppaz, M.: Influence of permafrost, rock and ice glaciers on chemistry of high-elevation ponds
- 1078 (NW Italian Alps), Science of the Total Environment, 685, 886–901, https://doi.org/10.1016/j.scitotenv.2019.06.233, 2019.
- 1079 Colucci, R. R., Forte, E., Žebre, M., Maset, E., Zanettini, C., and Guglielmin, M. Is that a relict rock glacier? Geomorphology,
- 1080 330, 177–189, https://doi.org/10.1016/j.geomorph.2019.02.002, 2019.

- 1081 Croce, F., and Milana, J.: Internal structure and behavior of a Rock Glacier in the arid Andes of Argentina, Permafrost and
- Periglacial Processes, 13, 289–299, <a href="https://doi.org/10.1002/ppp.431">https://doi.org/10.1002/ppp.431</a>, 2002.
- 1083 Del Siro, C., Scapozza, C., Perga, M.-E., & Lambiel, C.: Investigating the origin of solutes in rock glacier springs in the Swiss
- 1084 Alps: A conceptual model, Frontiers in Earth Science, 11, https://doi.org/10.3389/feart.2023.1056305, 2023.
  - Delaloye, R., Lambiel, C., and Gärtner-Roer, I.: Overview of rock glacier kinematics research in the Swiss Alps: Seasonal
- 1086 rhythm, interannual variations and trends over several decades, Geographica Helvetica, 65(2), 135-145,
- 1087 https://doi.org/10.5194/gh-65-135-2010, 2010.

- 1088 Dodds, C.J., and Campbell, R.B.: Overview, legend and mineral deposit tabulations for: GSC Open File 2188 to Open File
- 1089 2191, Geological Survey of Canada, Energy Mines and Resources Canada, 85 p. + 5 maps, 1992.
- 1090 Dugdale S. J.: A practitioner's guide to thermal infrared remote sensing of rivers and streams: recent advances, precautions
- and considerations, WIREs Water, vol. 3, no. 2, pp. 251–268, https://doi.org/10.1002/wat2.1135, 2016.
- 1092 Engel, M., Penna, D., Bertoldi, G., Vignoli, G., Tirler, W., and Comiti, F.: Controls on spatial and temporal variability in
  - streamflow and hydrochemistry in a glacierized catchment, Hydrology and Earth System Sciences, 23(4), 2041-2063,
- 1094 https://doi.org/10.5194/hess-23-2041-2019, 2019.
- 1095 Ensom, T., Makarieva, O., Morse, P., Kane, D., Alekseev, V., and Marsh, P.: The distribution and dynamics of aufeis in
- permafrost regions, Permafrost and Periglacial Processes, 31(3), 383–395, https://doi.org/10.1002/ppp.2051, 2020.
- 1097 Evin, M., Fabre, D., and Johnson, P. G.: Electrical Resistivity Measurements on the Rock Glaciers of Grizzly Creek, St Elias
- 1098 Mountains, Yukon, Permafrost and Periglacial Processes, 8, 11, 1997.
- 1099 Falatkova, K., Šobr, M., Slavík, M., Bruthans, J., and Janský, B.: Hydrological characterization and connectivity of proglacial
- 1100 lakes to a stream, Adygine ice-debris complex, northern Tien Shan, Hydrological Sciences Journal, 65(4), 610-623,
- 1101 https://doi.org/10.1080/02626667.2020.1711913, 2020.
- 1102 Frauenfelder, R., Allgöwer, B., Haeberli, W., and Hoelzle, M.: Permafrost investigations with GIS a case study in the
- 1103 Fletschhorn area, Wallis, Swiss Alps, In Permafrost, Proceedings of the Seventh International Conference, 23-27 June 1998,
- 1104 Yellowknife, Canada, Lewkowicz AG, Allard M (eds) eds, Collection Nordicana 57, Centre d'études Nordiques, Université
- 1 105 Laval: Québec; 291–295, 1998.
- 106 Gammons, C. H., Doolittle, M. F., Eastman, K. A., and Poulson, S. R.: Geochemistry of natural acid rock drainage in the Mt
- 107 Evans area, Anaconda Pintler Range, Montana, USA, Geochemistry: Exploration, Environment, Analysis, 21(4),
- 1 108 https://doi.org/10.1144/geochem2021-068, 2021.
- 1109 Gibson J.J., Holmes T., Stadnyk T.A., Birks S.J., Eby P., and Pietroniro A.: 18O and 2H in streamflow across Canada, Journal
- 1110 of Hydrology: Regional Studies, Volume 32, 100754, ISSN 2214-5818, https://doi.org/10.1016/j.ejrh.2020.100754, 2020.
- 1111 Haeberli, W.: Untersuchungen zur Verbreitung von Permafrost zwischen Flüelapass und Piz Grialetsch (Graubünden),
- 1112 Mitteilungen der VAW ETH Zürich 17: 1–221, 1975.

- 1113 Halla, C., Henrik Blöthe, J., Tapia Baldis, C., Trombotto Liaudat, D., Hilbich, C., Hauck, C., and Schrott, L.: Ice content and
- 1114 interannual water storage changes of an active rock glacier in the dry Andes of Argentina, Cryosphere, 15(2), 1187–1213,
- 1115 https://doi.org/10.5194/tc-15-1187-2021, 2021.
- 1116 Harrington, J. S., Mozil, A., Hayashi, M., and Bentley, L. R.: Groundwater flow and storage processes in an inactive rock
- 1117 glacier, Hydrological Processes, 32(20), 3070–3088, https://doi.org/10.1002/hyp.13248, 2018.
- 1118 Harrison, S., Jones, D., Anderson, K., Shannon, S., and Betts, R. A.: Is ice in the Himalayas more resilient to climate change
- 1119 than we thought? Geografiska Annaler, Series A: Physical Geography, 103(1), 1-7
- 1120 https://doi.org/10.1080/04353676.2021.1888202, 2021.
- 1121 Hayashi, M.: Alpine Hydrogeology: The Critical Role of Groundwater in Sourcing the Headwaters of the World. Groundwater,
- 1122 58(4), 498–510, https://doi.org/10.1111/gwat.12965, 2020.
- 1123 Hem, J. D.: Study and Interpretation of the Chemical Characteristics of Natural Water, 3rd Edition, US Geological Survey
- Water-Supply Paper 2254, University of Virginia, Charlottesville, 263 p., https://doi.org/10.3133/wsp2254, 1985.
- 1125 Hewitt, K.: Rock Glaciers and Related Phenomena. In K. Hewitt (Ed.), Glaciers of the Karakoram Himalaya: Glacial
- 1126 Environments, Processes, Hazards and Resources (pp. 267–289), Springer Netherlands, https://doi.org/10.1007/978-94-007-
- 1127 6311-1 11, 2014.
- Hock, R., Rasul, G., Adler, C., Cáceres, B., Gruber, S., Hirabayashi, Y., Jackson, M., Kääb, A., Kang, S., Kutuzov, S., Milner,
- 1129 Al., Molau, U., Morin, S., Orlove, B., and Steltzer, H.: High Mountain Areas. In: IPCC Special Report on the Ocean and
- 1130 Cryosphere in a Changing Climate [Pörtner, H.-O., Roberts, D.C., Masson-Delmotte, V., Zhai, P., Tignor, M., Poloczanska,
- 1131 E., Mintenbeck, K., Alegría, A., Nicolai, M., Okem, A., Petzold, J., Rama, B. and Weyer N.M. (eds.)]: Cambridge University
- 1132 Press, Cambridge, UK and New York, NY, USA, pp. 131-202, https://doi.org/10.1017/9781009157964.004, 2019.
- 1133 Hu, X., and Pollard, W.H.: The hydrologic analysis and modelling of river icing growth, North Fork Pass, Yukon Territory,
- 134 Canada, Permafrost and Periglacial Processes, 8: 279 294, https://doi.org/10.1002/(SICI)1099-1530(199709)8:3<279::AID-
- 1|135 <u>PPP260>3.0.CO;2-7, 1997.</u>
- Huss, M., Bookhagen, B., Huggel, C., Jacobsen, D., Bradley, R. S., Clague, J. J., Vuille, M., Buytaert, W., Cayan, D. r.,
- 1137 Greenwood, G., Mark, B. g., Milner, A. M., Weingartner, R., and Winder, M.: Toward mountains without permanent snow
- and ice, Earth's Future, 5(5), 418–435, https://doi.org/10.1002/2016EF000514, 2017.
- 1139 Iwasaki, K., Fukushima, K., Nagasaka, Y., Ishiyama, N., Sakai, M., and Nagasaka, A.: Real-Time Monitoring and
- 1140 Postprocessing of Thermal Infrared Video Images for Sampling and Mapping Groundwater Discharge, Water Resources
- 1141 Research, 59(4), e2022WR033630, https://doi.org/10.1029/2022WR033630, 2023.
- 1142 Iwasaki, K., Nagasaka Y., Ishiyama N., and Nagasaka A.: Thermal imaging survey for characterizing bedrock groundwater
- 1143 discharge: comparison between sedimentary and volcanic catchments, Hydrological Research Letters 18(3): 79-86,
- 1|144 <u>http://dx.doi.org/10.3178/hrl.18.79</u>, 2024.

- 1 45 Johnson, P. G.: Holocene Paleohydrology of the St. Elias Mountains, British Columbia and Yukon, Géographie Physique et
- 1 146 Quaternaire, 40(1), 47–53, https://doi.org/10.7202/032622ar, 1986.
- 1147 Johnson, P. G.: Mass Movement of Ablation Complexes and Their Relationship to Rock Glaciers, Geografiska Annaler, Series
- 1 48 A, Physical Geography, 56(1/2), 93 101, https://doi.org/10.2307/520430, 1974.
- 1149 Johnson, P. G.: Rock glacier types and their drainage systems, Grizzly Creek, Yukon Territory, Canadian Journal of Earth
  - Sciences, 15(9), 1496–1507, https://doi.org/10.1139/e78-155, 1978.
- 1151 Johnson, P. G.: Glacier Rock Glacier Transition in the Southwest Yukon Territory, Canada, Arctic and Alpine Research, 12(2),
- 1 1 1 5 2 195, https://doi.org/10.2307/1550516, 1980.

- 1153 Johnson, P. G.: Rock Glaciers, A Case for a Change in Nomenclature, Geografiska Annaler, Series A, Physical Geography,
- 1 1 54 65(1/2), 27 34, https://doi.org/10.2307/520718, 1983.
- 1055 Johnson, P. G.: Stagnant Glacier Ice, St. Elias Mountains, Yukon, Geografiska Annaler, Series A, Physical Geography, 74(1),
- 1 156 13 19, https://doi.org/10.2307/521466, 1992.
- 1157 Jones, D. B., Harrison, S., Anderson, K., and Betts, R. A.: Mountain rock glaciers contain globally significant water stores,
- Scientific Reports, 8(1), Article 1, https://doi.org/10.1038/s41598-018-21244-w, 2018.
- 1159 Jones, D. B., Harrison, S., Anderson, K., Shannon, S., and Betts, R. A.: Rock glaciers represent hidden water stores in the
- Himalaya, Science of The Total Environment, 793, 145368, https://doi.org/10.1016/j.scitotenv.2021.145368, 2021.
- Jones, D. B., Harrison, S., Anderson, K., and Whalley, W. B.: Rock glaciers and mountain hydrology: A review, Earth-Science
- Reviews, 193, 66–90, https://doi.org/10.1016/j.earscirev.2019.04.001, 2019.
- Kalbus, E., Reinstorf, F., and Schirmer, M.: Measuring methods for groundwater and surface water interactions: review,
- Hydrology and Earth System Sciences, 10(6), 873–887, https://doi.org/10.5194/hess-10-873-2006, 2006.
- 1165 Käser, D., and Hunkeler, D.: Contribution of alluvial groundwater to the outflow of mountainous catchments, Water Resources
- Research, 52(2), 680–697, https://doi.org/10.1002/2014WR016730, 2016.
- 1167 Krainer, K., and Mostler, W.: Hydrology of Active Rock Glaciers: Examples from the Austrian Alps, Arctic, Antarctic, and
- Alpine Research, 34(2), 142–149, https://doi.org/10.1080/15230430.2002.12003478, 2002.
- 1169 Krainer, K., Mostler, W., and Spötl, C.: Discharge from active rock glaciers, Austrian Alps: A stable isotope approach, Austrian
- 1170 Journal of Earth Sciences, 100, 102–112, 2007.
- 1171 Kummert, M., Bodin, X., Braillard, L., and Delaloye, R.: Pluri-decadal evolution of rock glaciers surface velocity and its
- 1172 impact on sediment export rates towards high alpine torrents, Earth Surface Processes and Landforms, 46(15), 3213–3227,
- 1173 https://doi.org/10.1002/esp.5231, 2021.
- 1 174 Liu, W., Fortier, R., Molson, J., and Lemieux, J.: A conceptual model for talik dynamics and icing formation in a river
- 1175 floodplain in the continuous permafrost zone at Salluit, Nunavik (Quebec), Canada, Permafrost and Periglacial Processes,
- 1 1 1 7 6 32(3), 468 483, https://doi.org/10.1002/ppp.2111, 2021.

Formatted: Border: Top: (No border), Bottom: (No border) Left: (No border), Right: (No border), Between: (No border)

- 1177 Lloyd, S.: Least squares quantization in PCM, IEEE Transactions on Information Theory, 28(2), 129–137, IEEE Transactions
- on Information Theory, <a href="https://doi.org/10.1109/TIT.1982.1056489">https://doi.org/10.1109/TIT.1982.1056489</a>, 1982.
- 1179 MacQueen, J.: Some methods for classification and analysis of multivariate observations, In Proceedings of the fifth Berkeley
- symposium on mathematical statistics and probability (Vol. 1, No. 14, pp. 281-297), 1967.
- 181 Mallinson, L., Swift, D. A., and Sole, A.: Proglacial icings as indicators of glacier thermal regime: Ice thickness changes and
- 182 icing occurrence in Svalbard, Geografiska Annaler, Series A: Physical Geography, 101(4), 334-349,
  - https://doi.org/10.1080/04353676.2019.1670952, 2019.

- 1184 Marcer, M., Cicoira, A., Cusicanqui, D., Bodin, X., Echelard, T., Obregon, R., and Schoeneich, P.: Rock glaciers throughout
- 1185 the French Alps accelerated and destabilised since 1990 as air temperatures increased, Communications Earth & Environment,
- 1186 2(1), 1–11, https://doi.org/10.1038/s43247-021-00150-6, 2021.
- 1187 Marren, P. M., and Toomath, S. C.: Channel pattern of proglacial rivers: Topographic forcing due to glacier retreat, Earth
- 1 Surface Processes and Landforms, 39(7), 943–951, https://doi.org/10.1002/esp.3545, 2014.
- 189 Müller, T., Lane, S. N., and Schaefli, B.: Towards a hydrogeomorphological understanding of proglacial catchments: An
- 190 assessment of groundwater storage and release in an Alpine eatehment, Hydrology and Earth System Sciences, 26(23), 6029-
- 1 191 6054, https://doi.org/10.5194/hess-26-6029-2022, 2022.
- 1192 Müller, T., Roncoroni, M., Mancini, D., Lane, S. N., and Schaefli, B.: Current and future roles of meltwater-groundwater
- dynamics in a proglacial Alpine outwash plain, Hydrology and Earth System Sciences, 28(4), 735-759,
- 1194 https://doi.org/10.5194/hess-28-735-2024, 2024.
- 1195 Navarro, G., Valois, R., MacDonell, S., de Pasquale, G., and Díaz, J. P.: Internal structure and water routing of an ice-debris
- 1196 landform assemblage using multiple geophysical methods in the semiarid Andes, Frontiers in Earth Science, 11,
- 1197 https://doi.org/10.3389/feart.2023.1102620, 2023.
- 1198 PERMOS Report 2019-16-19 | PERMOS Swiss Permafrost Monitorinig Network, Retrieved 17 September 2024, from
- 1199 https://www.permos.ch/doi/permos-rep-2019-16-19, 2019.
- 1200 Porter, C., Howat, I., Noh, M.-J., Husby, E., Khuvis, S., Danish, E., Tomko, K., Gardiner, J., Negrete, A., Yadav, B., Klassen,
- 1201 J., Kelleher, C., Cloutier, M., Bakker, J., Enos, J., Arnold, G., Bauer, G., and Morin, P.: ArcticDEM Mosaics, Version 4.1
- 1202 [Dataset], Harvard Dataverse, https://doi.org/10.7910/DVN/3VDC4W, 2023.
- 1203 Rautio, A., Kivimäki, A.-L., Korkka-Niemi, K., Nygård, M., Salonen, V.-P., Lahti, K., and Vahtera, H.: Vulnerability of
- 1204 groundwater resources to interaction with river water in a boreal catchment, Hydrology and Earth System Sciences, 19(7),
- 1205 3015–3032, https://doi.org/10.5194/hess-19-3015-2015, 2015.
- 1206 Reato, A., Borzi, G., Martínez, O. A., and Carol, E.: Role of rock glaciers and other high-altitude depositional units in the
- 1207 hydrology of the mountain watersheds of the Northern Patagonian Andes, Science of The Total Environment, 824, 153968,
- 1208 <u>https://doi.org/10.1016/j.scitotenv.2022.153968</u>, 2022.

- 1209 Robinson, C. T., Jolidon, C., Consoli, G., Bloem, S., and Ebi, C.: Temporal dynamics in the physico-chemistry of a high-
- alpine stream network in the Swiss National Park, Eco.Mont, 14(2), 11 23, https://doi.org/10.1553/eco.mont-14-2s11, 2022.
- 1211 Scapozza, C.: Contributo dei metodi termici alla prospezione del permafrost montano: esempi dal massiccio della Cima di
- 1212 Gana Bianca (Val Blenio, Svizzera), Bollettino della Società Ticinese di Scienze Naturali 97:55–66, 2009.
- 1213 Scapozza, C.: Investigation on protalus ramparts in the Swiss Alps, Geographica Helvetica, 70(2), 135-139,
- 1214 <u>https://doi.org/10.5194/gh-70-135-2015</u>, 2015.
- 1215 Schreder, S., Sommaruga, R., Psenner, R., Chimani, B., Ganekind, M., and Koinig, K. A.: Changes in air temperature, but not
- 1216 in precipitation, determine long-term trends in water chemistry of high mountain lakes of the Alps with and without rock
- 1217 glacier influence, Science of the Total Environment, 905, https://doi.org/10.1016/j.scitotenv.2023.167750, 2023.
- 1218 Scotti, R., Crosta, G. B., and Villa, A.: Destabilisation of Creeping Permafrost: The Plator Rock Glacier Case Study (Central
- 1219 Italian Alps), Permafrost and Periglacial Processes, 28(1), 224–236, https://doi.org/10.1002/ppp.1917, 2017.
- 1220 Sorg, A., Kääb, A., Roesch, A., Bigler, C., and Stoffel, M.: Contrasting responses of Central Asian rock glaciers to global
- warming, Scientific Reports, 5, <a href="https://doi.org/10.1038/srep08228">https://doi.org/10.1038/srep08228</a>, 2015.
- 1222 Terry, N., Grunewald, E., Briggs, M., Gooseff, M., Huryn, A. D., Kass, M. A., Tape, K. D., Hendrickson, P., and Lane, J. W.,
- 1223 Jr.: Seasonal Subsurface Thaw Dynamics of an Aufeis Feature Inferred From Geophysical Methods, Journal of Geophysical
- 1224 Research: Earth Surface, 125(3), https://doi.org/10.1029/2019JF005345, 2020.
- 1225 Tjoelker, A., Baraer, M., Valence, E., Charonnat, B., Masse-Dufresne, J., Mark, B., and McKenzie, J.: Drone-Based Ground-
- 1226 Penetrating Radar with Manual Transects for Improved Field Surveys of Buried Ice, Remote Sensing, 16, 2461,
- 1227 https://doi.org/10.3390/rs16132461, 2024.
- 1228 Toran, L.: Groundwater-Surface Water Interaction, In Encyclopedia of Water (pp. 1-12), John Wiley & Sons, Ltd,
- 1229 https://doi.org/10.1002/9781119300762.wsts0027, 2019.
- 1230 Torgersen C. E., Faux R. N., McIntosh B. A., Poage N. J., and Norton D. J.: Airborne thermal remote sensing for water
- 1231 temperature assessment in rivers and streams, Remote Sensing of Environment, vol. 76, no. 3, pp. 386-398,
- 1232 https://doi.org/10.1016/S0034-4257(01)00186-9, 2001.
- 1233 Tronstad, L. M., Hotaling, S., Giersch, J. J., Wilmot, O. J., and Finn, D. S.: Headwaters Fed by Subterranean Ice: Potential
- 1234 Climate Refugia for Mountain Stream Communities? Western North American Naturalist, 80(3), 395-407,
- 1235 https://doi.org/10.3398/064.080.0311, 2020.

- van Tiel, M., Aubry-Wake, C., Somers, L., Andermann, C., Avanzi, F., Baraer, M., Chiogna, G., Daigre, C., Das, S., Drenkhan,
  - F., Farinotti, D., Fyffe, C. L., de Graaf, I., Hanus, S., Immerzeel, W., Koch, F., McKenzie, J. M., Müller, T., Popp, A. L., ...
- 1238 Yapiyev, V.: Cryosphere-groundwater connectivity is a missing link in the mountain water cycle, Nature Water, 2(7), 624-
- 1239 637, https://doi.org/10.1038/s44221-024-00277-8, 2024.
- 1240 Vélez-Nicolás, M., García-López, S., Barbero, L., Ruiz-Ortiz, V., and Sánchez-Bellón, Á.: Applications of Unmanned Aerial
- 1241 Systems (UASs) in Hydrology: A Review, Remote Sensing, 13(7), Article 7, https://doi.org/10.3390/rs13071359, 2021.

- 1242 Wagner, T., Brodacz, A., Krainer, K., and Winkler, G.: Active rock glaciers as shallow groundwater reservoirs, Austrian Alps,
- 1243 Grundwasser, 25(3), 215–230, https://doi.org/10.1007/s00767-020-00455-x, 2020.
- 1244 Wagner, T., Kainz, S., Krainer, K., and Winkler, G.: Storage-discharge characteristics of an active rock glacier catchment in
- the Innere Ölgrube, Austrian Alps, Hydrological Processes, 35(5), https://doi.org/10.1002/hyp.14210, 2021.
- 1246 Wagner, T., Pauritsch, M., and Winkler, G.: Impact of relict rock glaciers on spring and stream flow of alpine watersheds:
- 1247 Examples of the Niedere Tauern Range, Eastern Alps (Austria), Austrian Journal of Earth Sciences, 109(1),
- 1248 https://doi.org/10.17738/ajes.2016.0006, 2016.
- 1249 Wahl, H. E., Fraser, D. B., Harvey, R. C., and Maxwell, J. B.: Climate of Yukon, Atmospheric Environment Service,
- 1250 Environment Canada, 1987.
- 1251 Wainstein, P., Moorman, B., and Whitehead, K.: Glacial conditions that contribute to the regeneration of Fountain Glacier
- 1252 proglacial icing, Bylot Island, Canada, Hydrological Processes, 28(5), 2749—2760, https://doi.org/10.1002/hyp.9787, 2014.
- 1253 Wanner, C., Moradi, H., Ingold, P., Cardenas Bocanegra, M. A., Mercurio, R., and Furrer, G.: Rock glaciers in the Central
- 1254 Eastern Alps How permafrost degradation can cause acid rock drainage, mobilization of toxic elements and formation of
- basaluminite, Global and Planetary Change, 227, https://doi.org/10.1016/j.gloplacha.2023.104180, 2023.
- 1256 Webb, B. W., Hannah, D. M., Moore, R. D., Brown, L. E., and Nobilis, F.: Recent advances in stream and river temperature
- research, Hydrological Processes, 22(7), 902–918, https://doi.org/10.1002/hyp.6994, 2008.
- 1258 Winkler, G., Wagner, T., Pauritsch, M., and Kellerer-Pirklbauer, A.: What will occur after permafrost? Relevance of relict
- 1259 rock glaciers for the discharge behaviour of alpine catchments, Joannea Geologie und Palaontologie, 12, 63-72, 2016.
- 1260 Zappa C. J., Jessup A. T., and Yeh H.: Skin layer recovery of free-surface wakes: Relationship to surface renewal and
- dependence on heat flux and background turbulence, Journal of Geophysical Research: Oceans, vol. 103, no. C10, pp. 21711
- 1262 21722, 1998, https://doi.org/10.1029/98JC01942, 1998.
- 1263 Zarroca, M., Roqué, C., Linares, R., Salminci, J. G., and Gutiérrez, F.: Natural acid rock drainage in alpine catchments: A side
- 1264 effect of climate warming, Science of The Total Environment, 778, 146070, https://doi.org/10.1016/j.scitotenv.2021.146070,
- 1265 2021.
- 1266 Zierl, B., and Bugmann, H.: Global change impacts on hydrological processes in Alpine catchments, Water Resources
- 1267 Research, 41(2), https://doi.org/10.1029/2004WR003447, 2005.